

1 **The very-high resolution configuration of the**
2 **EC-Earth global model for HighResMIP**

3
4
5 Eduardo Moreno-Chamarro^{1,2*}, Thomas Arsouze^{1,3}, Mario Acosta¹, Pierre-Antoine Bretonnière¹,
6 Miguel Castrillo¹, Eric Ferrer¹, Amanda Frigola¹, Daria Kuznetsova¹, Eneko Martin-Martinez¹,
7 Pablo Ortega¹, Sergi Palomas¹

- 8
9
10 1. Barcelona Supercomputing Center (BSC), Barcelona, Spain
11 2. Now at: Max Planck Institute for Meteorology, Hamburg, Germany
12 3. Now at: CIRAD, UMR AMAP, F-34398 Montpellier, France
13 * Corresponding author: eduardo.chamarro@mpimet.mpg.de

31 **Abstract**

32 We here present the very-high resolution version of the EC-Earth global climate model, EC-
33 Earth3P-VHR, developed for HighResMIP. The model features an atmospheric resolution of ~16
34 km and an oceanic resolution of $1/12^\circ$ (~8 km), which makes it one of the finest combined
35 resolutions ever used to complete historical and scenario-like CMIP6 simulations. To evaluate
36 the influence of numerical resolution on the simulated climate, EC-Earth3P-VHR is compared
37 with two configurations of the same model at lower resolution: the ~100-km-grid EC-Earth3P-
38 LR, and the ~25-km-grid EC-Earth3P-HR. Out of the three configurations, VHR shows the
39 smallest drift in the global mean ocean temperature and salinity at the end of a 100-year 1950's
40 control simulation, which points to a faster equilibrating phase than in LR and HR. In terms of
41 model biases, we compare the historical simulations against observations over the period 1980–
42 2014. In contrast to LR and HR, VHR shows a reduced equatorial Pacific cold tongue bias, an
43 improved Gulf Stream representation, with a reduced coastal warm bias and a reduced subpolar
44 North Atlantic cold bias, and more realistic orographic precipitation over mountain ranges. By
45 contrast, VHR shows a larger warm bias and overly low sea ice extent over the Southern Ocean.
46 Such biases in surface temperature have an impact on the atmospheric circulation aloft,
47 connected with more realistic stormtrack over the North Atlantic, yet less realistic stormtrack
48 over the Southern Ocean compared to the lower resolution model versions. Other biases persist
49 or worsen with increased resolution from LR to VHR, such as the warm bias over the tropical
50 upwelling region and the associated cloud cover underestimation, a precipitation excess over the
51 tropical South Atlantic and North Pacific, and an overly thick sea ice and an excess in oceanic
52 mixing in the Arctic. VHR shows improved air–sea coupling over the tropical region, although it
53 tends to overestimate the oceanic influence on the atmospheric variability at mid-latitudes
54 compared to observations and LR and HR. Together, these results highlight the potential for
55 improved simulated climate in key regions, such as the Gulf Stream and the Equator, when the
56 atmospheric and oceanic resolutions are finer than 25 km in both the ocean and atmosphere.
57 Thanks to its unprecedented resolution, EC-Earth3P-VHR offers a new opportunity to study
58 climate variability and change of such areas on regional/local spatial scales, in line with regional
59 climate models.

60

61

62 1. Introduction

63 Interest in high-resolution modeling has soared in the past years, specially thanks to large
64 European research projects and initiatives such as [PRIMAVERA](#) (PRIMAVERA and the
65 European Commission, 2015), [nextGEMS](#) (Hohenegger et al., 2023, Rackow et al., 2024),
66 [EERIE](#), and [Destination Earth](#) (Hoffmann et al., 2023) (last access: 20 June 2024). Broadly,
67 these projects seek to build the next generation of high-resolution global climate (or Earth
68 system) models capable of representing climate phenomena with unprecedented accuracy, to
69 simulate and predict regional climate, guide policymaking, and provide relevant climate
70 information to end users. Thanks to these efforts, high-resolution models at resolutions of 25–50
71 km or even finer have been proven to lead to reduced biases in the simulated climate (see
72 Introduction in Moreno-Chamarro et al., 2022 for a review), and to a better representation of, for
73 example, tropical cyclones (Roberts et al., 2020a; Vidale et al., 2021; Zhang et al., 2021), storm-
74 tracks (e.g., Hodges et al., 2011), the intertropical convergence zone (ITCZ; e.g., Doi et al.,
75 2012; Tian et al., 2020), or the Gulf Stream and associated air–sea interactions (e.g., Kirtman et
76 al., 2012; Bellucci et al., 2021) compared to standard resolution models (hereafter, ~100-km
77 grid). An extensive review of the benefit of high-resolution modeling can be found in Haarsma et
78 al. (2016), Hewitt et al. (2017), Roberts M.J. et al. (2018), and Czaja et al. (2019). However,
79 increased model resolution alone is not always the answer: for example, persistent, well-known
80 biases in clouds and radiation can be insensitive to an increase in atmospheric resolution from a
81 ~100-km grid to a 25–50-km grid (Moreno-Chamarro et al., 2022). Inadequate model physics or
82 insufficient tuning can thus mask or negate the benefits of increased resolution.

83 High-resolution modeling faces additional challenges. One is the high computational cost of
84 running the simulations, and another, related, is the difficulty of achieving high throughput due
85 to the loss of efficiency with increasing parallelization. These issues have gradually improved
86 thanks to steady increases in supercomputing power and parallel enhancements in model
87 efficiency to leverage that power. The community trusts in High Performance Computing (HPC)
88 to increase the performance of climate models, developing different approaches to speed models
89 up. These approaches can go from improving the traditional parallelization algorithms (Tintó
90 Prims et al., 2019a) or reducing the accuracy of the variables from double to single precision
91 (Váña et al., 2017, Tintó Prims et al., 2019b) to increasing the Input/Output throughput of
92 complex model configurations (Xepes-Arbós et al., 2022, Sarmany et al., 2024). Faster models

93 are also needed to complete, in a reasonable time, the tuning and the spin-up phases, which for a
94 high-resolution model, can be extremely costly. The demand for high efficiency in high-
95 resolution modeling has therefore accelerated the development and implementation of new
96 modeling strategies to ensure an optimal use of the computing resources.

97 High-resolution models also need to find a fair compromise between the resolutions of the
98 different climate components, which, sometimes, can be very disparate—for example, an eddy-
99 rich ocean model (~10 km grid) coupled to a 25 km, 50 km, or even coarser-grid atmosphere
100 model (e.g., Gutjahr et al., 2019, Rackow et al., 2019, Semmler et al., 2020). Tsartsali et al.
101 (2022), for example, reported increased ocean–atmosphere coupling strength and better
102 agreement with reanalysis and observations over the Gulf Stream, when both the ocean and
103 atmosphere resolutions are increased to comparable ~25-km grid at least. Moreton et al. (2021)
104 showed a degraded representation of the air–sea interaction at increased oceanic resolution but a
105 constant atmospheric resolution. Similarly, Ma et al. (2016) found that the mesoscale ocean
106 temperature affects the storm track over the Pacific only when the atmospheric model resolution
107 is enough to resolve the small-scale diabatic heating. Finally, Rai et al. (2023) described a
108 disproportionate eddy killing when a coarse 200-km wind forcing is used to force a finer (~10–
109 25-km) ocean, compared to the case with similar grid sizes. These results of these studies thus
110 advocate for a similar resolution in both the atmosphere and ocean.

111 Sometimes, high-resolution modeling relies on single-model component, either atmospheric-
112 only (Baker et al., 2019) or ocean-only configurations (e.g., Biastoch et al., 2021), or on regional
113 models (e.g., Woollings et al., 2010; Ma et al., 2017) as in CORDEX (Jacob et al., 2014) for
114 hypothesis testing and downscaling climate projections. Such configurations, however, lack
115 global energy constraints, remote influences, and, potentially, key feedbacks rectifying the mean
116 state. These models are also limited by the boundary conditions, which often are derived from
117 coarser (~100 km) global models and can present biases in their mean climate that might be
118 absent or much reduced at a higher resolution; these biases might then be passed onto the single
119 model configurations. For example, an overly smooth Gulf Stream temperature gradient, an
120 incorrect separation, or the lack of mesoscale in ocean temperatures can impact the response of
121 the atmospheric circulation aloft (e.g., Ma et al., 2017; Lee et al., 2018). Low-resolution and
122 high-resolution global models can also respond differently to climate change: for example, the
123 northward shift and strong surface warming of the Gulf Stream projected by the eddy-rich

124 configuration of the HadGEM3-GC3.1 model for the 21st century is absent at the lower-
125 resolution model versions (Moreno-Chamarro et al., 2021). Associated with this, the increase in
126 winter precipitation is similarly much larger over Europe at the highest resolution than at any
127 lower one, which reinforces the idea that the response of the atmosphere is strongly sensitive to
128 the boundary conditions. These findings put a limit to our confidence in single-model
129 configurations and regional models, since they lack a global dynamical response.

130 As a response to the listed challenges, we here present the eddy-rich version of the EC-Earth
131 climate model for PRIMAVERA/HighResMIP. This is likely one of the finest combined
132 horizontal resolution global models ever used to complete CMIP-like simulations, with a
133 nominal resolution of about 10–15 km; it also has the additional advantage that the resolution is
134 comparable in both the atmosphere and ocean/sea-ice, which allows the atmosphere to “see” the
135 fine-scale forcing from the ocean with minimal information lost from interpolation. In this paper,
136 we describe the model configuration and the developments in model efficiency (Section 2), as
137 well as the main characteristics of its climate for the period 1980–2014 compared to observations
138 (Section 3).

139

140 **2. Model Description and Experimental Setup**

141 ***2.1 Model description***

142 All HighResMIP contributions with the EC-Earth global coupled climate model have been
143 performed with its version 3.2.2, developed within the PRIMAVERA project (EC-Earth3P). The
144 model consists of atmosphere, ocean, and sea ice components. The atmosphere model is based
145 on the ECMWF Integrated Forecasting System (IFS), in the 36r4 cycle (based on IFS system 4,
146 [https://www.ecmwf.int/sites/default/files/elibrary/2011/11209-new-ecmwf-seasonal](https://www.ecmwf.int/sites/default/files/elibrary/2011/11209-new-ecmwf-seasonal-forecast-system-system-4.pdf)
147 [-forecast-system-system-4.pdf](https://www.ecmwf.int/sites/default/files/elibrary/2011/11209-new-ecmwf-seasonal-forecast-system-system-4.pdf), last access: 8 November 2024). A detailed account of the changes
148 introduced in this cycle can be found on the ECMWF website
149 (<https://confluence.ecmwf.int/display/FCST/Implementation+of+IFS+Cycle+36r4>, last access:
150 20 June 2024). The very-high resolution version of the model, EC-Earth3P-VHR, features a
151 triangular truncation at wave number 1279 (hence known as T1279) in spectral space, with a
152 linear N640 reduced Gaussian grid. This corresponds to a spacing of ~16 km. However, because
153 of the complexity of numerical solutions and parametrizations, the effective resolution (this is the
154 smallest scale IFS T1279 can fully resolve) is of ~120 km (Abdalla et al., 2013). Vertically, the

155 model features 91 levels, resolving the middle atmosphere up to 0.01 hPa. The model time step
156 during the simulation was 360 s. IFS integrates the revised land surface hydrology Tiled
157 ECMWF Scheme for Surface Exchanges over Land (H-Tessel) model (Balsamo et al., 2009;
158 Hazeleger et al., 2012).

159 The ocean model is the Nucleus for European Modelling of the Ocean in its version 3.6
160 (NEMO3.6; Madec, 2008, Madec and the NEMO team, 2016). This is a hydrostatic, finite-
161 difference, free-surface, primitive equation general circulation model. EC-Earth3P-VHR uses the
162 ORCA12 tripolar grid, with the horizontal resolution increasing from the Equator to the poles:
163 ~9 km at the Equator, ~7 km at mid-latitudes, and ~2 km near the poles. This corresponds to an
164 effective resolution of ~45 km (roughly five times the ORCA grid spacing; Soufflet et al., 2016).
165 The model uses a z^* coordinate system for the vertical grid and has 75 vertical levels, with the
166 resolution decreasing from 1 m at the surface to 200 m in the deep ocean. The bottom
167 topography is derived from the combination of ETOPO1 (Amante and Eakins, 2009) and
168 GEBCO_08 (Becker et al., 2009). VHR does not include an ocean current feedback (Renault et
169 al., 2023). The sea ice model is the Louvain-la-Neuve sea Ice Model in its version 3 (LIM3)
170 (Vancoppenolle et al., 2012). This is a dynamic-thermodynamic sea ice model, with five ice
171 thickness categories. The time steps are 240 s for NEMO3.6, and 720 s for LIM3 in the EC-
172 Earth3P-VHR.

173 The atmosphere–land and ocean–sea-ice components are coupled through the OASIS
174 (Ocean, Atmosphere, Sea Ice, Soil) coupler, version 3 (OASIS-MCT 3.0) (Valcke and Morel,
175 2006; Craig et al., 2017). OASIS remaps the atmosphere fluxes onto the ocean grid via nearest-
176 neighbor distance-based Gauss-weighted interpolation. The exchange includes the transfer of
177 momentum, energy, and mass fluxes from the atmosphere to the ocean, while sea-surface
178 temperature and sea ice and snow variables from the ocean to the atmosphere. The remapping of
179 runoff from the atmospheric grid points to runoff areas on the ocean grid was re-implemented to
180 be independent of the grid resolution. This was done by introducing an auxiliary model
181 component and relying on the interpolation routines provided by the OASIS coupler. More
182 details on the coupling are provided by Döscher et al. (2022).

183 EC-Earth3P-VHR (hereafter, VHR) is compared with two lower-resolution global model
184 versions, also run within the PRIMAVERA/HighResMIP project: EC-Earth3P (hereafter, LR;
185 EC-Earth Consortium, 2019), and EC-Earth3P-HR (hereafter, HR; EC-Earth Consortium, 2018).

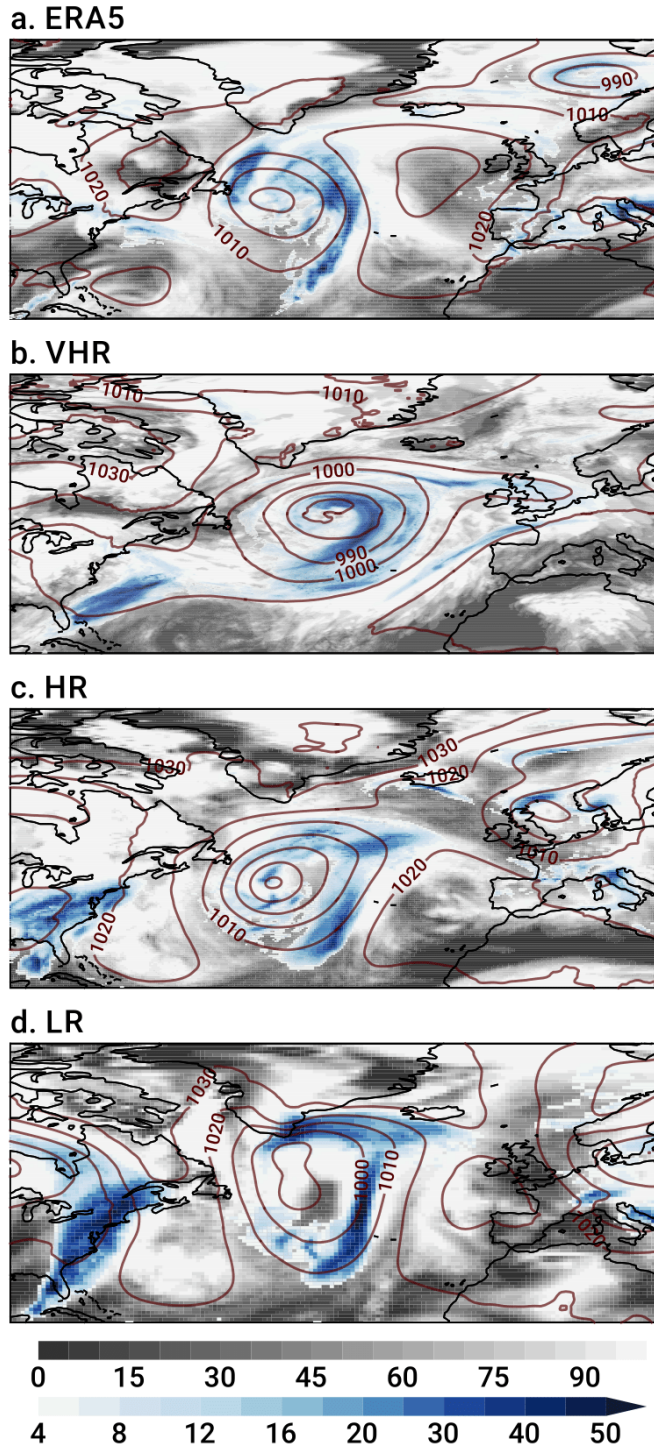
186 In the atmosphere, they use the T255 (~107 km) and T511 (~54.2 km) spectral resolution of the
187 IFS model respectively (equivalent to an effective resolution of ~600 km and ~280 km
188 respectively; Abdalla et al., 2013), both with 91 vertical levels. In the ocean, LR and HR use the
189 ORCA1 (~100 km) and ORCA025 (~25 km) tripolar grid respectively (equivalent to an effective
190 resolution of ~500 km and ~125 km respectively; Soufflet et al., 2016), both with 75 vertical
191 levels. They both use the LIM3 sea ice model and the OASIS coupler as well. LR and HR's time
192 steps are respectively 2700 s and 900 s in all the atmosphere, ocean, and sea ice. More details of
193 these two other model versions can be found in Haarsma et al. (2020).

194 Following the CMIP6 HighResMIP protocol, no additional tuning is applied across
195 resolutions but for a short list of parameters that explicitly change with resolution, particularly
196 for oceanic diffusion and viscosity. The higher resolution in the atmosphere results in a better
197 representation of features such as tropical storms, land/sea transitions, heavy rainfall, and fronts
198 (see Fig. 1 as an example), while in the ocean the increase in resolution allows mesoscale
199 processes to be resolved at a much larger range of latitudes and the representation of finer
200 resolution bathymetric features and coastlines.

201 ***2.2 Configuration and workflow setup and performance optimization***

202 The development and maintenance of the EC-Earth model is supported by the EC-Earth
203 Consortium, which shares model code, configurations, and minimal software infrastructure to
204 operate it. While the LR and HR configurations of EC-Earth-3P were developed in a broad
205 collaboration of all the consortium members participating in PRIMAVERA, VHR's development
206 was primarily completed at the Barcelona Supercomputing Center, in collaboration with the
207 Swedish Meteorological and Hydrological Institute (SMHI) within the [ESiWACE2](#) H2020
208 project (last access: 20 June 2024). The development was conducted on two different
209 supercomputing machines: [MareNostrum3](#), and [MareNostrum4](#) (last access: 20 June 2024).
210 VHR's configuration, at the time of the project, represented one of the most cutting-edge
211 versions of a climate model to run over long time scales. Obtaining a production version of the
212 model, however, entailed i) generating new grid files; ii) deploying the initial data; iii) generating
213 the coupling weights (see below); iv) creating a new namelist for the ocean NEMO model; v)
214 modifying the runscripts to handle the new files and new configuration; vi) bringing changes
215 from modern versions of the model workflow (Auto-EC-Earth), which, for example, automatizes
216 the call of ELPiN (Tintó et al., 2017; Haarsma et al., 2020) and lets the user fine-tune the

217 distribution of the computational resources in parallel systems; vii) updating the XIOS (the
218 library for input/output management; <https://forge.ipsl.jussieu.fr/ioserver>, last access; 30 October
219 2024) to deal with the land suppression; and viii) exploring and modifying the configuration
220 parameters to improve the computational throughput of the model execution without losing result
221 accuracy (see below). This presented a significant challenge for both the operations department
222 and the workflow developers, which were required to fine-tune the system to achieve stable runs
223 and minimize the loss of computing hours. Moreover, generating the interpolation weight files to
224 couple the new model grids for the OASIS coupler was particularly challenging. This process
225 could not readily be parallelized at that time in VHR's OASIS3-MCT coupler version (in
226 contrast to more recent ones), and it required collaborating with the OASIS development group.
227 For the workflow, a significant proportion of the effort was devoted to exploiting the hybrid
228 architecture and integrating the dedicated data transfer nodes available in the MareNostrum4
229 cluster into the workflow software. Additionally, the automatic algorithm that enables the
230 suppression of land grid subdomains in the NEMO ocean model (ELPiN; Tintó et al., 2017) was
231 incorporated, resulting in a reduction of about 12% in the required HPC resources (see Haarsma
232 et al., 2020 for more details). Finally, the MareNostrum4 new network (100Gb Intel Omni-Path
233 Full-Fat Tree), despite its fast and responsive nature, proved to be quite unstable when subjected
234 to high workloads involving multiple concurrent communications, as was the case of the VHR
235 configuration. However, despite the significant challenges, at the end of the ESiWACE2 project
236 (December 2022), the configuration was ready and all the code was versioned and shared with
237 the other partners within the EC-Earth Consortium.



238

239

240 **Figure 1.** Snapshot of an extratropical storm over the North Atlantic in the winter 1999–2000 in
 241 a) ERA5, and in the b) VHR, c) HR, and d) LR models on their original grids. Shown are daily
 242 precipitation rate (mmd^{-1} ; blue shading), cloud cover (% of area; gray shading), and sea-level
 243 pressure (hPa; contours).

244 Once deployed, the workflow needed to be made more efficient to be put into operation.
245 Emerging advancements in global climate modeling demand heightened focus on HPC,
246 particularly to accommodate the increasing need for enhanced model resolution (Acosta et al.,
247 2024). An example of such demanding requirements is the VHR configuration, underscoring the
248 need for efficient resource use. In order to address this issue, we conducted a two-fold HPC
249 performance exercise, which involved both a pure computational performance analysis and a
250 scalability study for each model component (IFS and NEMO), complemented with a load
251 balance optimization for the coupling. This analysis concluded that the coupling and output
252 process could be a bottleneck. An optimization was included to package different coupling fields
253 to be sent in the same MPI (Message Passing Interface) communications, reducing the latency
254 and taking advantage of the bandwidth. Additionally, the I/O (Input/Output) setup was optimized
255 to ensure minimal time was needed to produce the outputs.

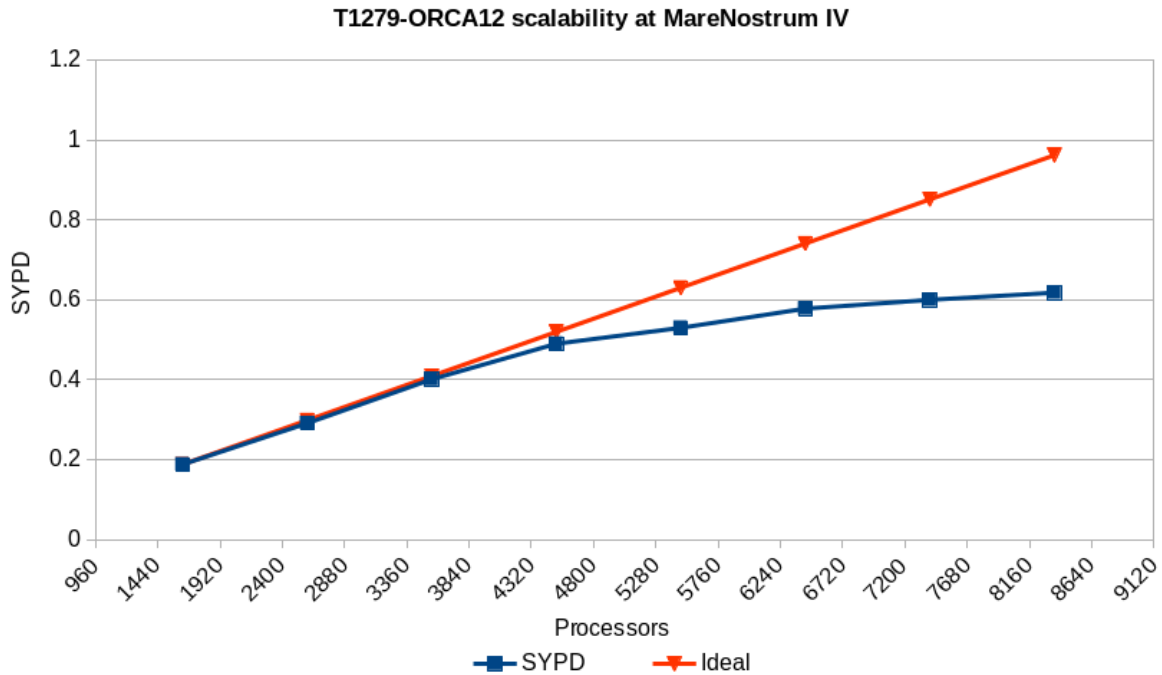
256 While the primary objective of the scalability and load-balance study was to assess the
257 model's efficiency and determine an optimal resource utilization, findings by Acosta et al. (2023)
258 also indicate that enhancing the performance of one component, such as reducing the execution
259 time of IFS, may not necessarily decrease the overall execution time of the coupled model. This
260 discrepancy could stem from a synchronization point at the end of each coupled time step, where
261 both components exchange fields. In cases where other non-optimized components lag behind, a
262 load rebalance becomes necessary.

263 Concerning the scalability exercise, we ran a series of tests to balance the resources
264 (computing cores) of the VHR's IFS and NEMO models (Fig. 2). To find the most balanced
265 configuration for a given amount of resources, we followed two different but complementary
266 approaches. The first and most costly one tried to find the optimal distribution by assigning the
267 same number of processors to IFS and NEMO first, and moving resources between them
268 alternately; this allowed identifying the intervals for which the model performance increases by
269 using variations of half-interval search algorithm. The second approach to balance the
270 configuration started from one separate scalability test for each model component that was later
271 used to determine the optimal configuration.

272

273

274



275
 276 **Figure 2.** Results of the scalability test of the VHR configuration (T1279 IFS and ORCA12
 277 NEMO) at MareNostrum4 (blue line) in simulated years per day (SYPD) for a given amount of
 278 processors. The orange line shows the ideal case with no loss in computing performance.

279
 280 The workflow software Auto-EC-Earth and, by extension, the simulations described here
 281 were configured and run with the workflow manager Autosubmit (Manubens-Gil et al., 2016).
 282 This Python package facilitates the production of numerical experiments, like the EC-Earth ones,
 283 and it allows easily handling experiments with different members, start dates, and initial
 284 conditions. The workflow is an oriented graph that includes pre- and post-processing data, the
 285 transfer to storage spaces, or the conversion of the output data to CMOR standard, with details
 286 on computing resources needed for each step.

287 **2.3 Simulations**

288 The VHR simulations follow the HighResMIP experimental protocol (Haarsma et al., 2016) and
 289 consist of: i) a 50-year spin-up run (spin-up-1950), with initial conditions of temperature and
 290 salinity from an ocean state representative of the 1950s (Good et al., 2013, EN4 data set) and
 291 forcing consisting of well-mixed greenhouse gases, including O₃ and aerosol loading for a
 292 1950s (~10-year mean) climatology; ii) a 105-year control run (control-1950),

293 starting from the end of spin-up-1950 and keeping the same fixed forcing; iii)
294 the historical run (hist-1950), starting from the same initial state as the control,
295 but with time-varying external forcing for the period 1950–2014; iv) and the
296 future scenario run (highres-future), as a continuation of the historical
297 simulation under the CMIP6 SSP5-8.5 scenario (Kriegler et al., 2017) for the
298 period 2015–2050. In this work, VHR's hist-1950 simulation is compared with
299 corresponding hist-1950 runs from LR and HR (Haarsma et al., 2020).

300 During the model setup, we erroneously applied the EN4 initial conditions at the beginning
301 of all the spin-up runs. While EN4 uses practical salinity and potential temperature, the NEMO
302 model, which uses the TEOS-10 equation of state, requires absolute salinity and conservative
303 temperature. Nonetheless, the differences between the two temperature and salinity types is
304 indeed small (Pawlowicz, 2013; McDougall et al., 2021), and we expect the error to minimize
305 throughout the spin-up (see Section 3.1).

306

307 ***2.4 Observations and reanalysis***

308 As we mainly aim to evaluate the performance of EC-Earth3P-VHR configuration and describe
309 the main model biases and characteristics, we focus on the best-observed part of the historical
310 period of the historical simulations, between 1980 and 2014. The three model configurations are
311 compared with the following observational and reanalysis data: near-surface (2 m) air
312 temperature (SAT), zonal winds, sea-level pressure, and turbulent fluxes from the ERA5
313 reanalysis (Hersbach et al., 2020); precipitation rate from the version-2 GPCP dataset (Adler et
314 al., 2003); cloud cover from the version-3 ESA Cloud_cci dataset (ESA CCI-CLOUD; Stengel et
315 al., 2020); potential temperature and salinity of the ocean from the Hadley Center EN4 (version
316 4.2.2; Good et al., 2013); sea ice concentration from OSI SAF (OSI-409/OSI-409-a;
317 EUMETSAT Ocean and Sea Ice Satellite Application Facility, 2015); and sea ice volume from
318 GIOMAS (Global Ice-Ocean Modeling and Assimilation System; Zhang and Rothrock, 2003).
319 The period of comparison maximizes data availability and is therefore 1980–2014 for all the
320 cases, except for the GPCP dataset (1983–2014) and the ESA CCI-CLOUD dataset (1982–2014).

321 Biases in sea-surface temperature (SST) are very similar to those in SAT and are therefore not
322 shown.

323

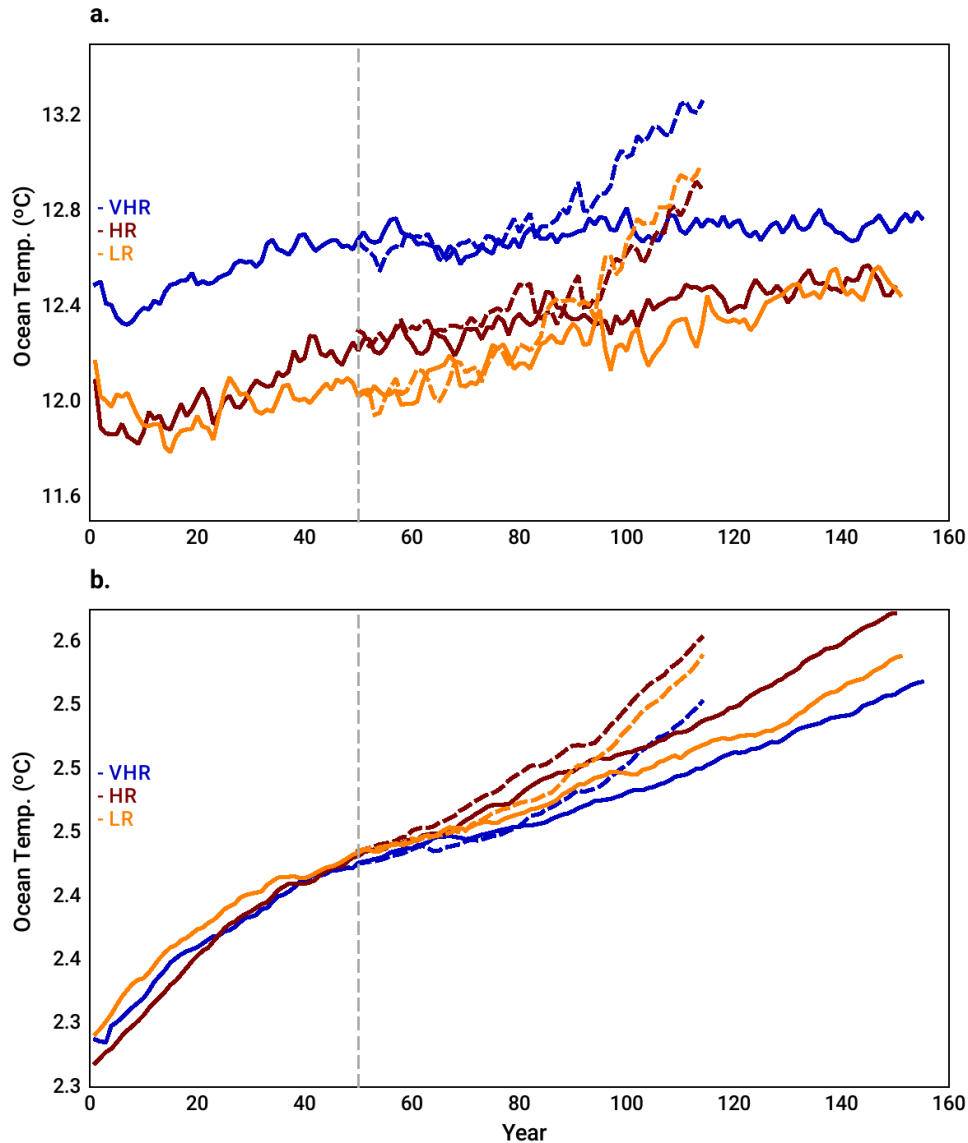
324 **3. Results**

325 **3.1 Spin-up phase**

326 Across all three model resolutions, the length of the spin-up (50 years) appears to be insufficient
327 to equilibrate the full ocean (Fig. 3b); in fact; the ocean temperature is still drifting about 0.001–
328 0.002 °C/yr (computed over the last 50 years) towards warmer conditions at the end of the
329 control simulation in the three configurations. In the upper ocean, however, VHR shows the
330 smallest warming drift of the three configurations: about 0.00005 °C/yr compared to 0.0025
331 °C/yr and 0.0062 °C/yr in HR and LR, respectively (computed over the last 50 years; Fig. 3a). It
332 is therefore safe to say that an analysis focused on the upper ocean and on the air–sea interface
333 will feature a relatively stable climate in the control simulations. In the historical simulations, the
334 warming of the ocean accelerates due to the CO₂ forcing; after 64 years (year 114 in Fig. 3), the
335 whole ocean warming reaches similar values to those at the end of the control simulations after
336 100 years in the three model resolutions. Near the surface, the warming trend is much larger. Of
337 the three configurations, VHR is the one with the smallest drift in the control run and the
338 smallest ocean warming in the historical period. Although the three runs start from similar initial
339 conditions derived from an EN4 climatology (Section 2.3), VHR is ~0.4 °C warmer near the
340 surface than LR and HR, especially over the spin-up period. This is likely related to the
341 development of a widespread warm bias over the Southern Ocean (Fig. 4), which we discuss in
342 detail in Section 3.6. The trends in global salinity at the end of the control simulations are all
343 smaller than 0.00005 psu/yr (computed over the last 50 years; not shown); the three
344 configurations are thus still drifting slightly. As found for the temperature, VHR also shows the
345 smallest drifts out of the three configurations (not shown).

346 In the following Sections, we describe the main characteristics of the VHR compared to LR
347 and HR by focusing on particular regions and biases. This approach should help us highlight the
348 benefits, or lack thereof, due to increased resolution. The main biases in the three model
349 configurations are compared with the observational data set listed in Section 2.4.

350



351
 352 **Figure 3.** Mean oceanic temperature (in °C) in the LR (yellow), HR (red), and VHR (blue)
 353 models in the spin-up runs (0–50-year period), control runs (50–150-year period; solid lines),
 354 and historical runs (50–114-year period; dashed lines) in a) the upper 100 m, and b) the whole
 355 ocean. The vertical dashed line marks the end of the spin-up period.

356
 357 **3.2 Tropics**

358 A warm bias of 1–2 K is present over the subtropical upwelling regions along the South
 359 American and African coasts in the three configurations and shows small variations across them
 360 (Fig. 4). The increase in resolution in VHR has thus no clear benefit to reduce it. Past studies
 361 have related this bias to an underestimation of the stratocumulus cloud deck (Richter, 2015). This

362 also seems to be the case in the three models, which all show negative cloud biases by about 20
363 % over all the subtropical upwelling areas, specially along the subtropical Pacific and Atlantic
364 western coasts (Fig. 5). A better resolved orography near the region does not contribute to
365 reducing the bias either, as suggested in previous studies (Milinski et al., 2016): for example,
366 although VHR shows reduced temperature biases along the Andes compared to HR and LR, it
367 has no effect on the biases over the eastern subtropical Pacific upwelling.

368 Overall, VHR shows reduced tropical precipitation biases compared to HR and LR (Fig. 6).
369 This is the case, for example, for the double ITCZ bias: this bias is usually characterized by a
370 precipitation excess over the central tropical North Pacific and the western tropical South Pacific
371 and a precipitation deficit over the equatorial Pacific, as LR clearly shows. The dry area over the
372 Equator is reduced with resolution, and the anomaly is even non-significant in VHR. This is a
373 clear improvement from increased resolution, and it can be related to a reduced cold bias over
374 the Equator (Fig. 4). In contrast, the precipitation excess over the tropical North Pacific and the
375 Maritime Continent persists into VHR, with only minor reductions of 1–2 mmd^{-1} compared to
376 HR and LR (Fig. 6). The precipitation excess over the tropical North Pacific suggests a seasonal
377 cycle reaching too far north, while the excess over the Maritime Continent, together with that
378 over the western tropical Atlantic and Indian oceans, suggests an excess in convective
379 precipitation over very warm waters.

380 Over the tropical Atlantic, the precipitation bias pattern points to an ITCZ anchored to the
381 south-western part and not reaching the Sahel area. This bias is somewhat reduced in VHR
382 compared to HR and LR, although not entirely removed. Over land, the dry bias over North
383 Brazil, which has been linked to a misrepresentation of the seasonal cycle and extreme events in
384 CMIP6 models (Monteverde et al., 2022), as well as the wet bias along the Andes are not
385 reduced with resolution, either. These positive and negative precipitation biases appear together
386 with positive and negative biases in cloud cover, respectively, related to an overestimation or
387 underestimation in convective clouds (Fig. 5).

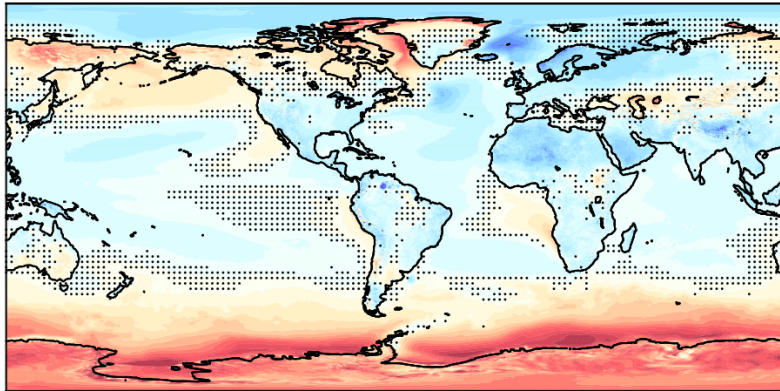
388

389

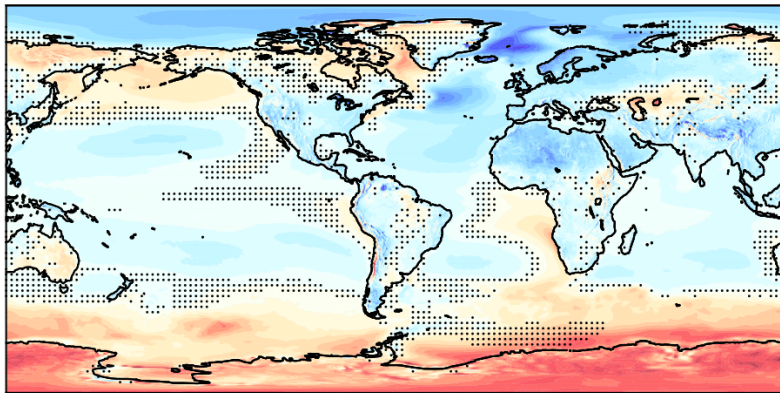
390

391

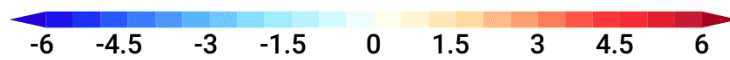
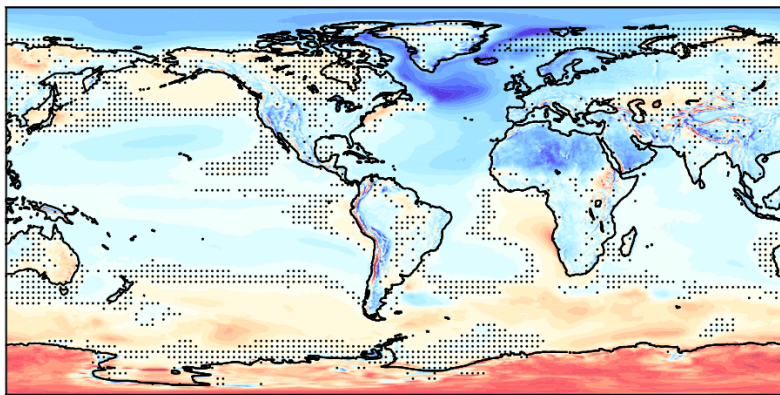
a. VHR



b. HR

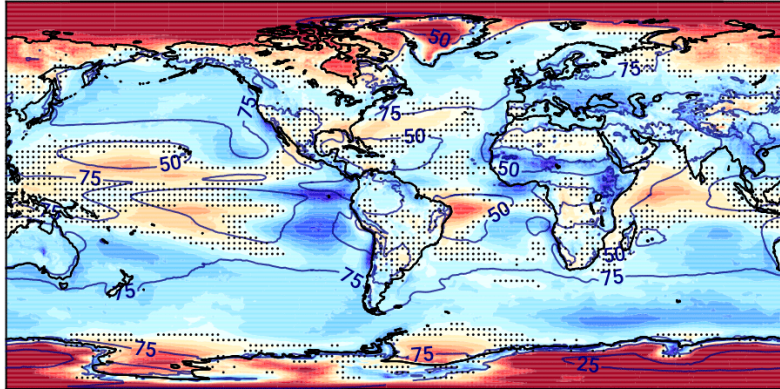


c. LR

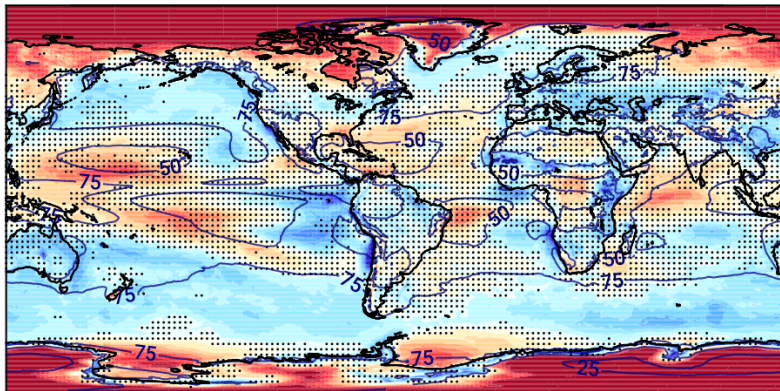


392
393 **Figure 4.** Bias in SAT (in K) with respect to ERA5 in the a) VHR, b) HR, and c) LR models for
394 the period 1980–2014. Stippling masks anomalies that are not significant at the 5 % level.
395

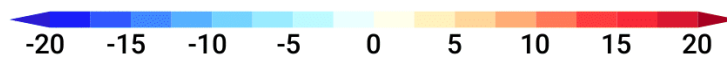
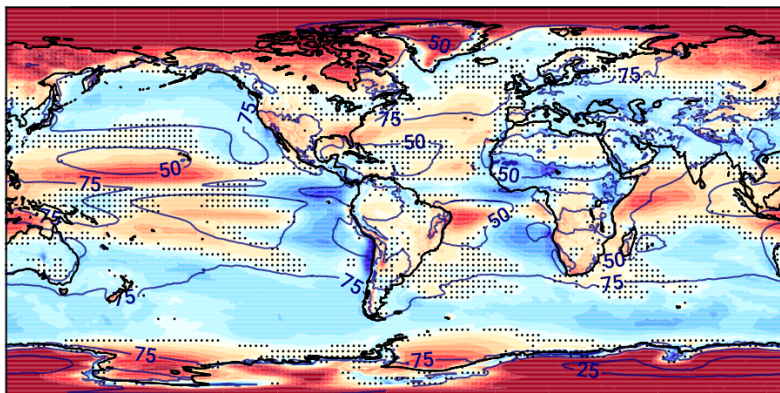
a. VHR



b. HR



c. LR



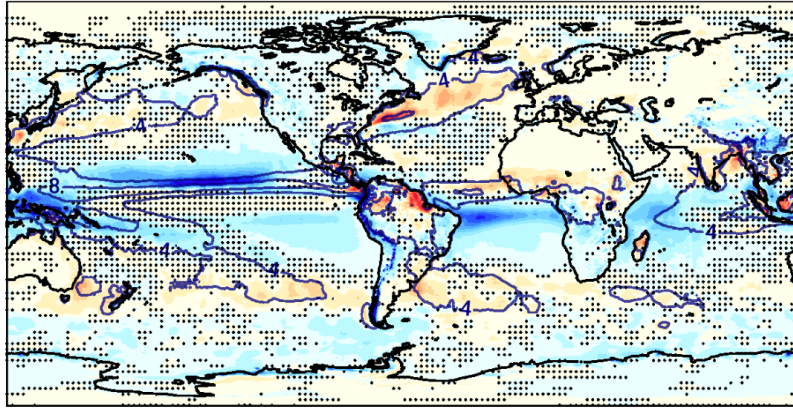
396

397 **Figure 5.** Bias in cloud cover (in %) with respect to ESA CCI-CLOUD (contours in all the

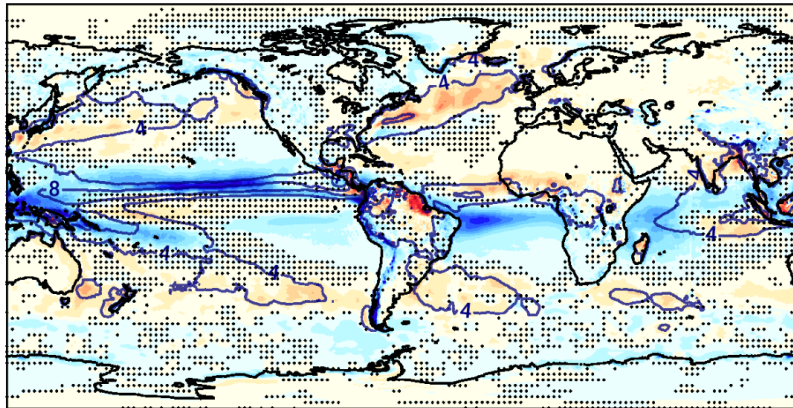
398 panels; in %) in the a) VHR, b) HR, and c) LR models for the period 1982–2014. Stippling

399 masks anomalies that are not significant at the 5 % level.

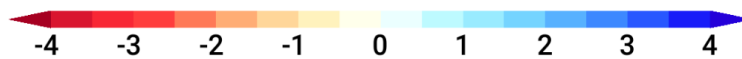
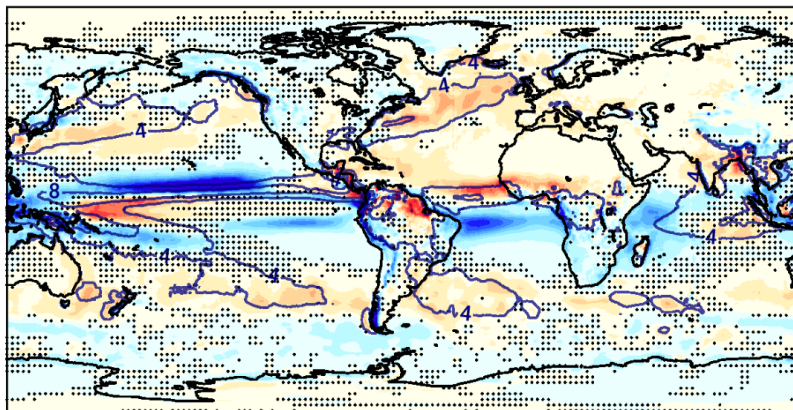
a. VHR



b. HR



c. LR



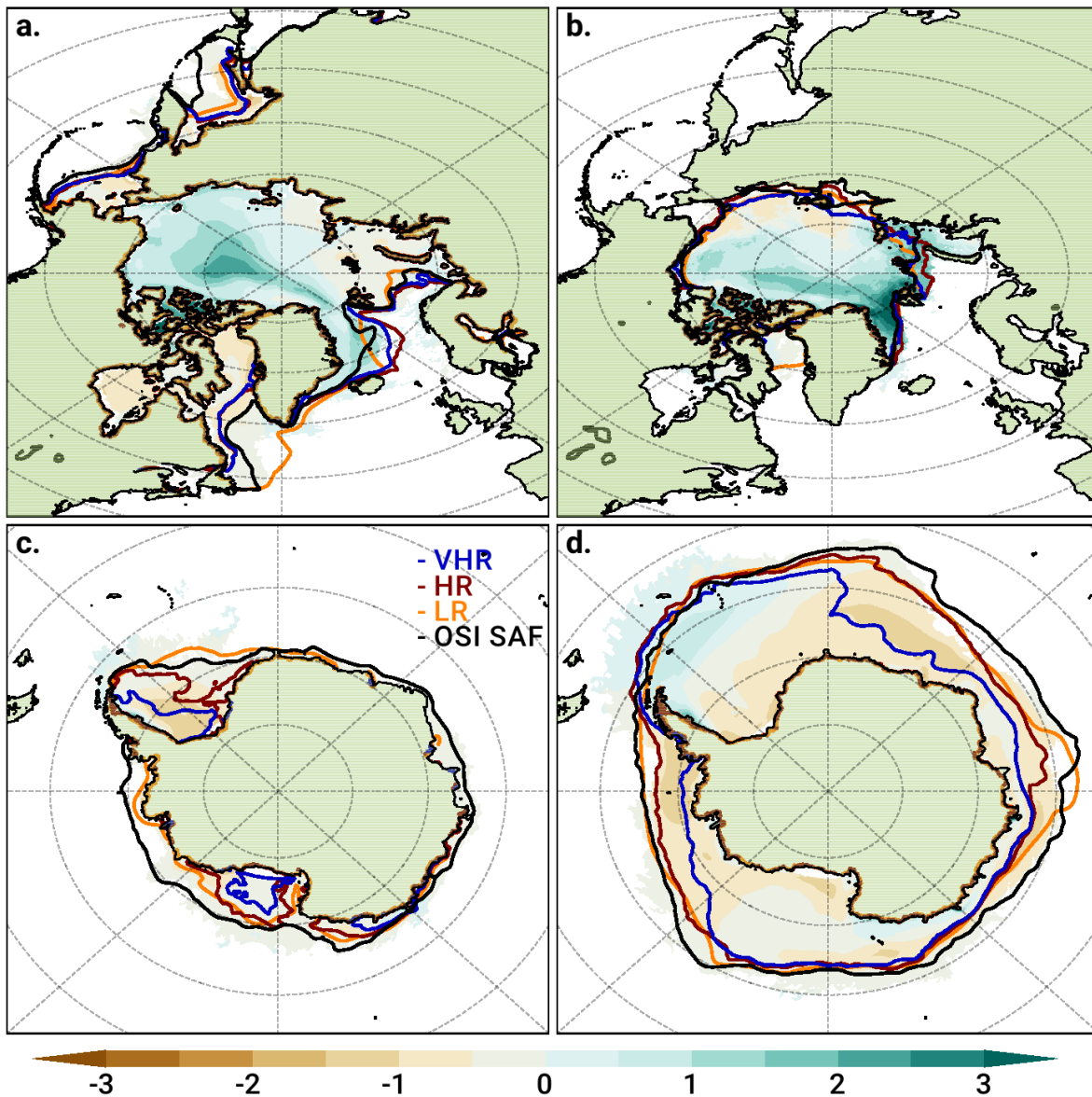
400
401 **Figure 6.** Bias in precipitation rate (in mmd^{-1}) with respect to GPCP (contours in all the panels;
402 in mmd^{-1}) in the a) VHR, b) HR, and c) LR models for the period 1983–2014. Stippling masks
403 anomalies that are not significant at the 5 % level.

404 **3.3 Northern Hemisphere mid- and high-latitudes**

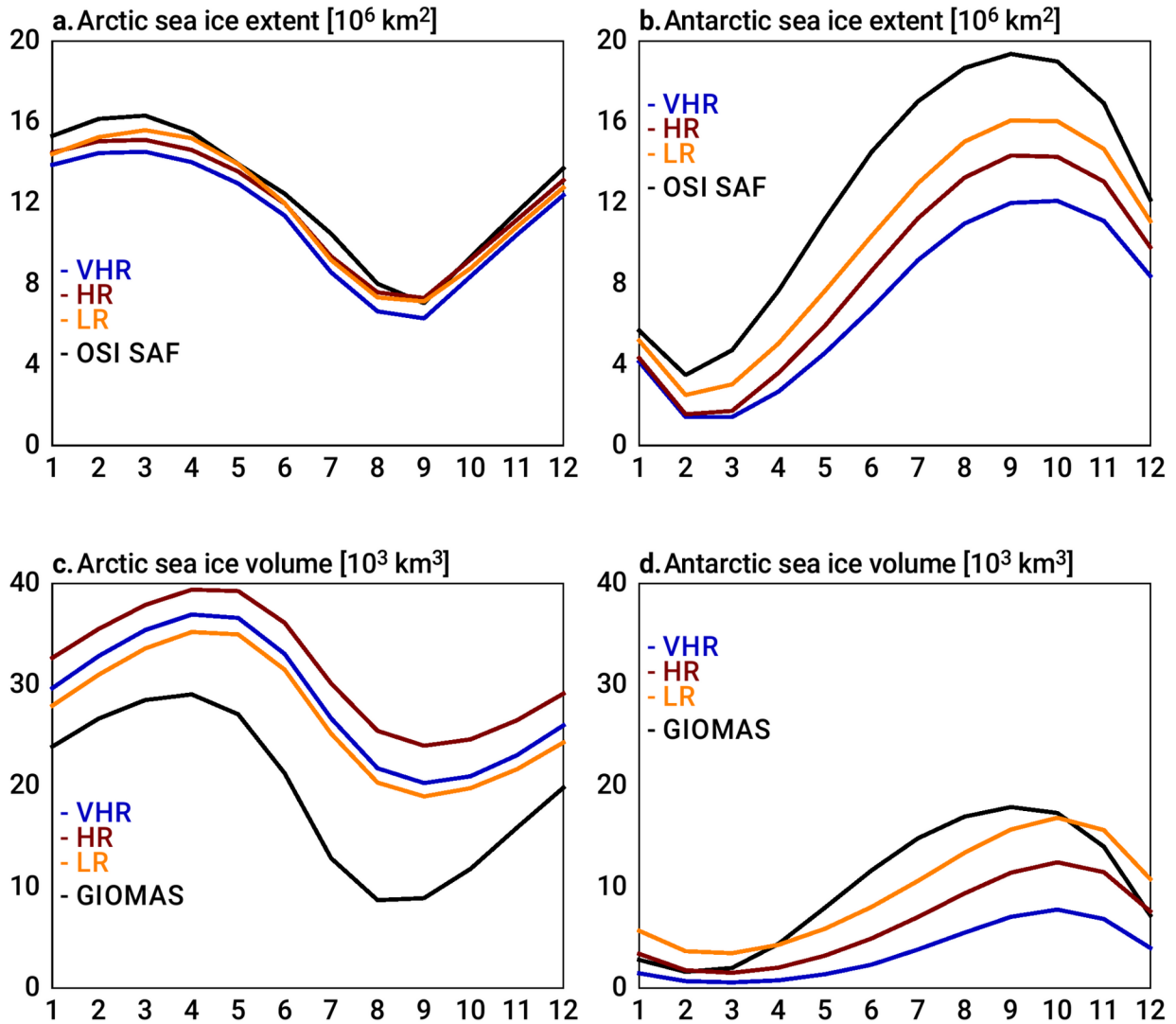
405 The largest improvement in the simulated climate from LR to VHR is over the North Atlantic.
406 From south to north, the Gulf Stream representation is much improved in VHR compared to HR
407 and LR, with sharper gradients in temperature and sea-surface height (not shown). The position
408 of the Gulf Stream separation is also improved, which leads to a reduction of the warm bias
409 along the US East Coast from LR to VHR (Fig. 4). A paper on a dedicated analysis of the biases
410 over the North Atlantic along the Gulf Stream is currently in preparation.

411 Farther north, the widespread cold bias up to about 6 K in LR is strongly reduced in HR, and
412 even further in VHR, which is the configuration closest to observations (Fig. 4). The cold bias in
413 LR is related to an unrealistically large sea ice extent, which covers the entire Labrador Sea and
414 the western part of the subpolar North Atlantic (Figs. 7 and 8). The reduction of the cold bias
415 between LR and VHR has a deep impact on the climate of the North Atlantic. In the atmosphere
416 aloft, it improves the representation of the boreal winter (DJF) stormtrack (Fig. 9) and jet (Fig.
417 10). The boreal winter stormtrack is overestimated over the subpolar North Atlantic, particularly
418 over the eastern part, in LR, likely related to an excessively strong meridional temperature
419 gradient; by contrast, VHR stormtrack is much closer to ERA5 over the North Atlantic. In the
420 ocean, excessive sea ice leads to a negative salinity bias above 2 psu in the subpolar North
421 Atlantic in LR, which is much reduced in VHR (Fig. 11). Two mechanisms can explain this fresh
422 bias in LR: on the one hand, a reduced oceanic salinity transport from subtropical latitudes by a
423 weakened subpolar gyre (not shown); on the other, errors in the seasonal cycle of the sea ice,
424 during which ice melting would cause an anomalous freshwater input in regions where it is not
425 observed. The negative bias in surface salinity propagates into deeper levels, especially between
426 300 m and 1000 m in the Arctic (Fig. 12). Similarly, the warm subsurface bias at around 40–50
427 °N might also be related to the sea ice excess in the subpolar North Atlantic in LR (Fig. 11).
428 Expanded sea ice in LR causes weaker subpolar gyre strength and associated northward heat
429 transport (not shown), leading to heat accumulation in the intergyre region. However, although
430 this bias is reduced at higher resolutions in HR and VHR, it is still present, suggesting other
431 deficiencies in the formation of intermediate waters in the North Atlantic. The overly large sea
432 ice cover also hampers oceanic deep mixing in the Labrador Sea in LR, whose main region of
433 deep water formations are in the Nordic Seas instead (Fig. 13). Oceanic deep mixing takes larger
434 values above 1000 m in VHR and HR in the Labrador Sea. A detailed analysis of the

435 characteristics and driving mechanisms of the deep water formation in the Labrador Sea across
436 the three resolutions and compared to observations is currently in preparation.

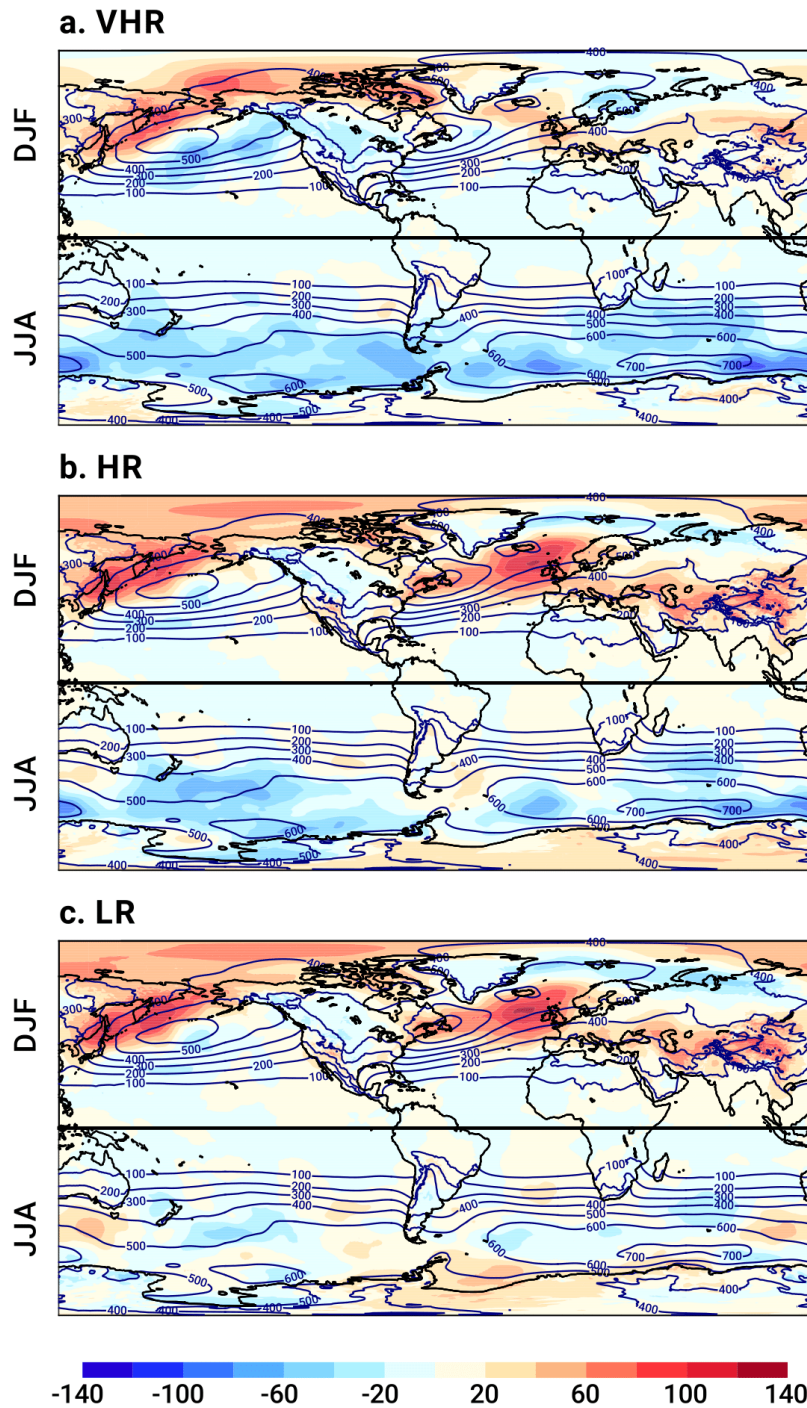


437
438 **Figure 7.** Bias in sea ice thickness (in m; shading) in VHR with respect to GIOMAS for the
439 period 1980–2014. Colored contours are the 15-% value of the sea ice concentration in the LR
440 (orange), HR (red), and VHR (blue) models, as well as in OSI SAF (black) for the period 1980–
441 2014. (a,b) are for the Arctic, while (c,d) are for Antarctica in March (a,c) and September (b,d).

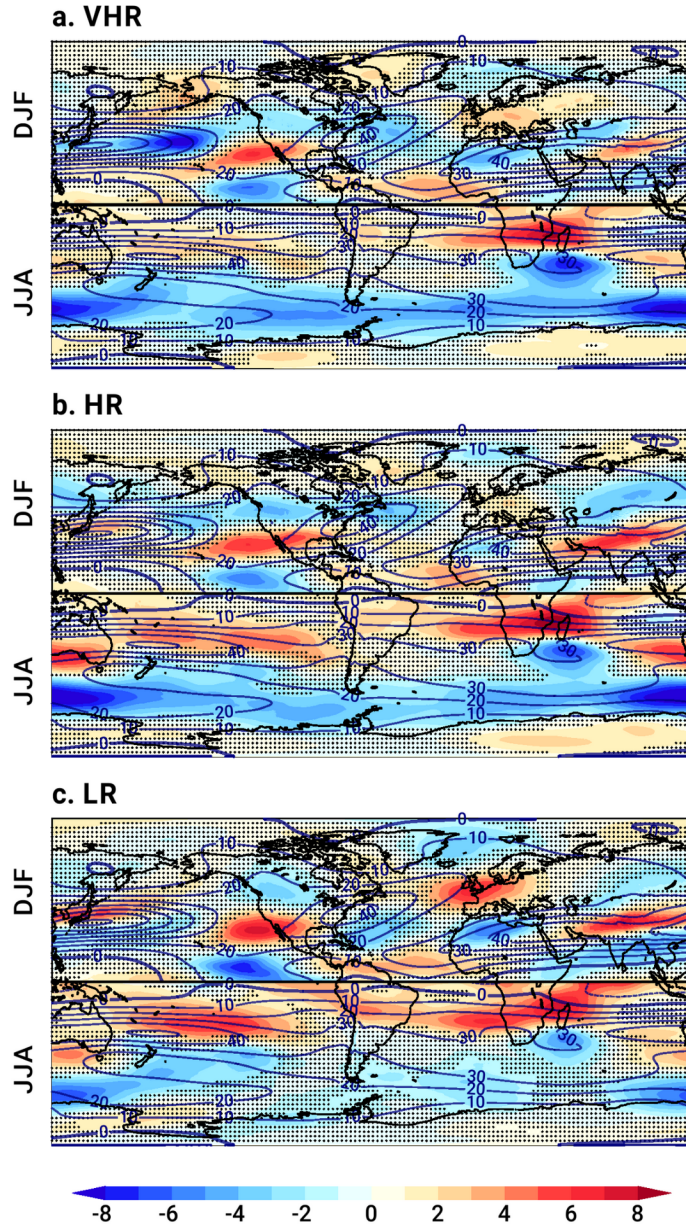


442
 443 **Figure 8.** Monthly climatology in the sea ice extent (in 10^6 km^2 ; a,b) and volume (in 10^3 km^3 ;
 444 c,d) in the Arctic (left) and Antarctica (right) in the LR (yellow), HR (red), and VHR (blue)
 445 models, as well as in OSI SAF, for sea ice extent, and GIOMAS, for the volume, for the period
 446 1980–2014.

447
 448
 449
 450
 451
 452

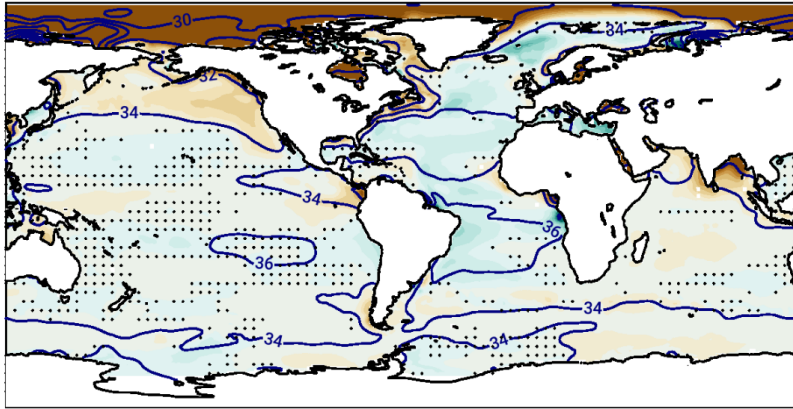


453
 454 **Figure 9.** Bias in winter stormtrack, computed as the standard deviation of the 2–6 d band-pass
 455 filtered daily sea-level pressure (in Pa) with respect to ERA5 (contours in all the panels; in Pa) in
 456 the a) VHR, b) HR, and c) LR models for the period 1980–2014. Each panel show anomalies in
 457 the boreal winter (DJF; top) and austral winter (JJA; bottom).

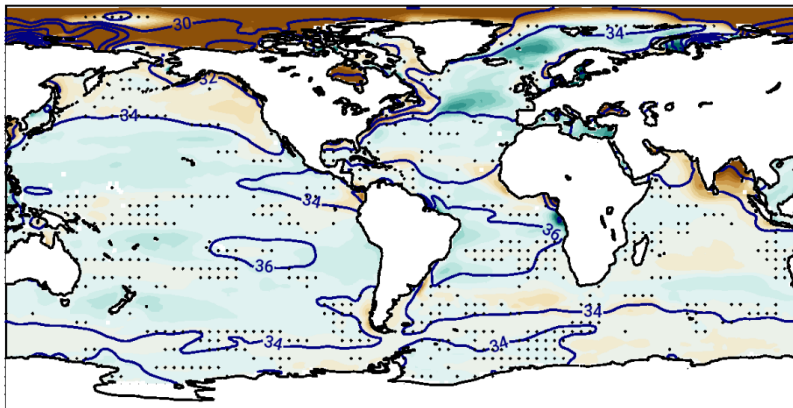


458
 459 **Figure 10.** Bias in winter zonal wind at 250 hPa (in ms^{-1}) with respect to ERA5 (contours in all
 460 the panels; in ms^{-1}) in the a) VHR, b) HR, and c) LR models for the period 1980–2014. Stippling
 461 masks anomalies that are not significant at the 5 % level. Each panel show anomalies in the
 462 boreal winter (DJF; top) and austral winter (JJA; bottom).

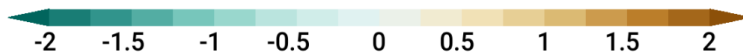
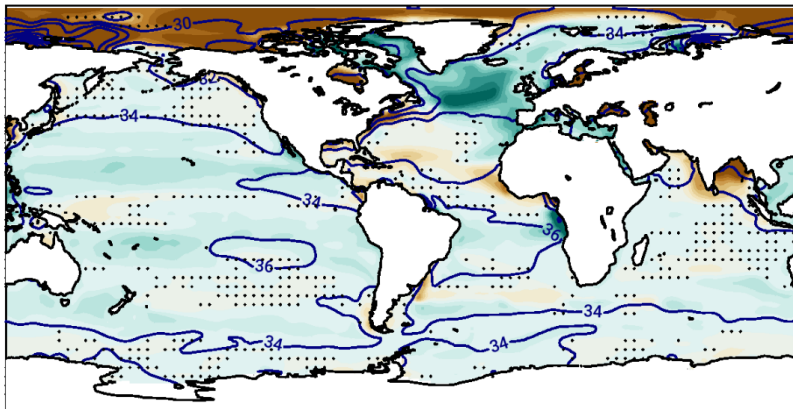
a. VHR



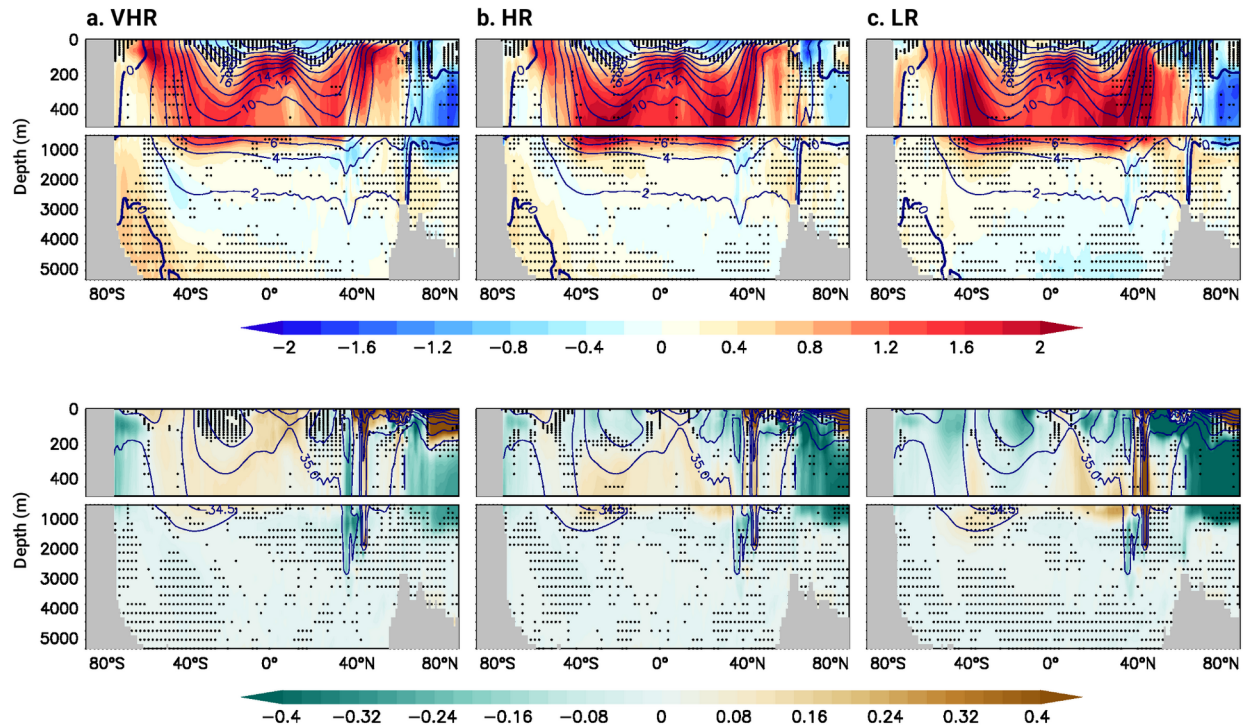
b. HR



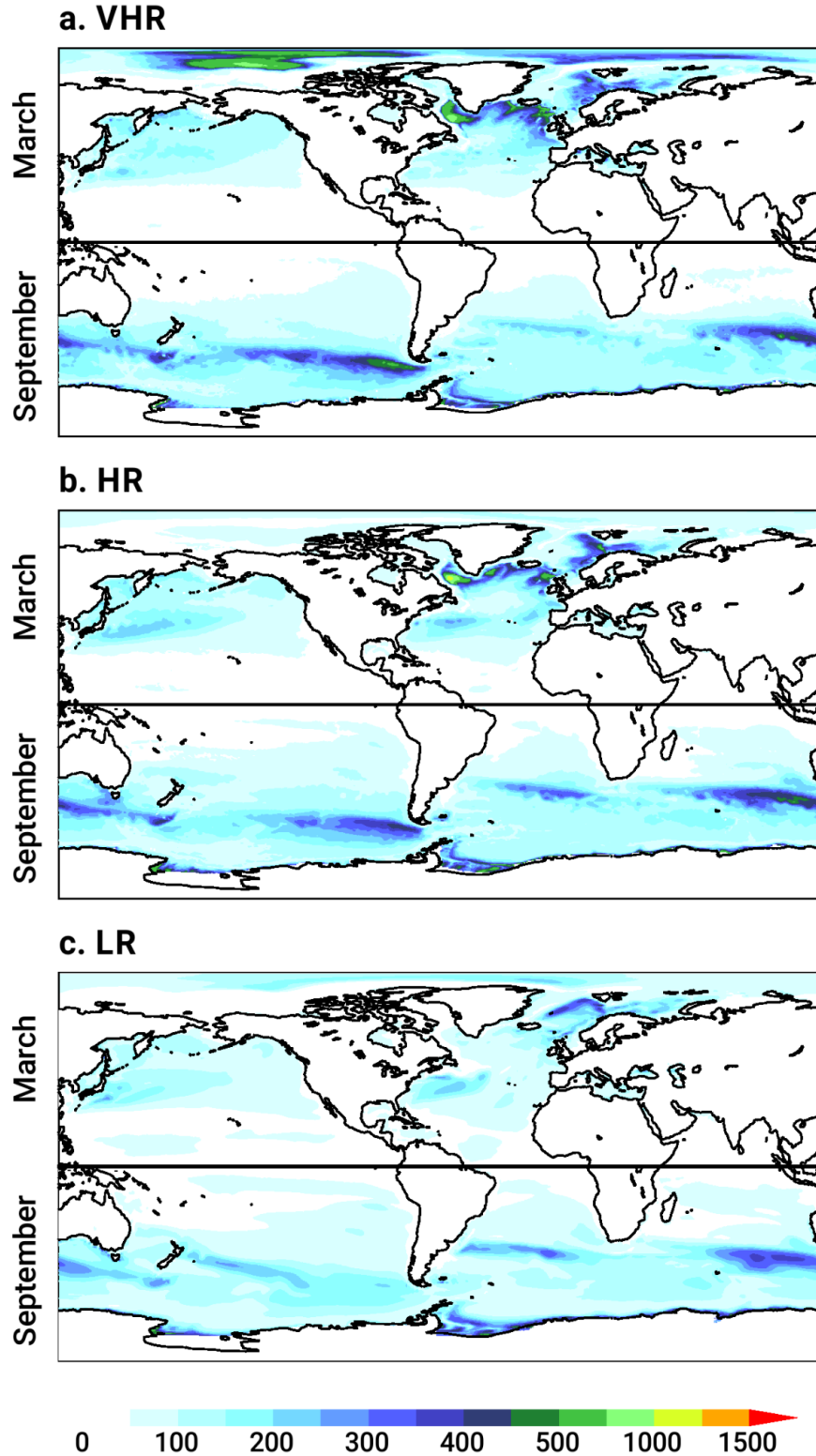
c. LR



463
464 **Figure 11.** Sea-surface salinity bias (in psu) with respect to EN4 (contours in all the panels; in
465 psu) in the a) VHR, b) HR, and c) LR models for the period 1980–2014. Stippling masks
466 anomalies that are not significant at the 5 % level.

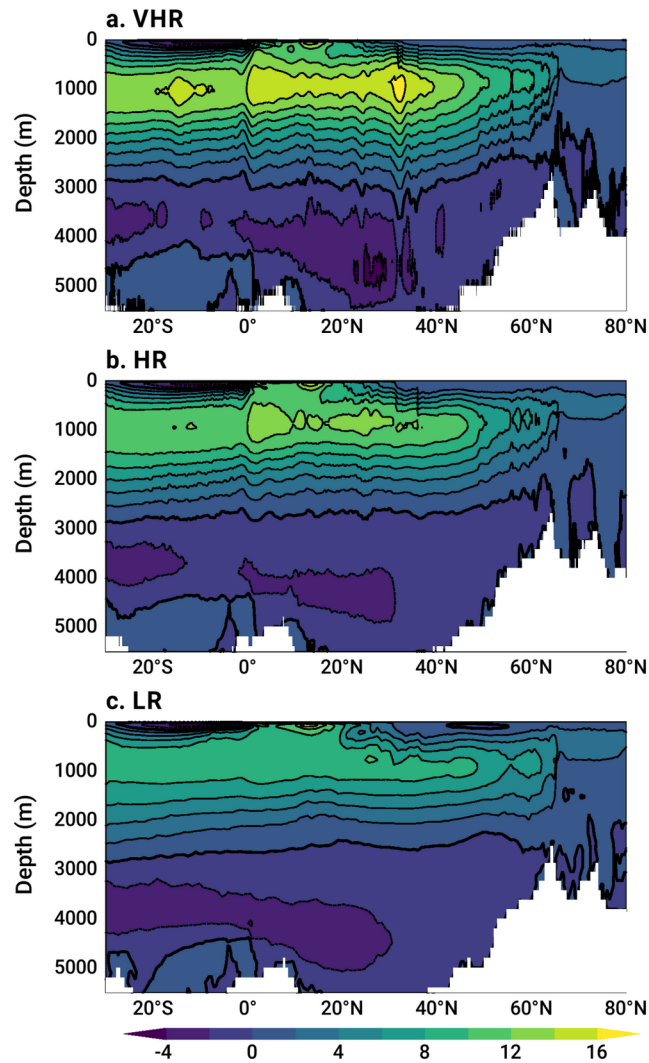


467
 468 **Figure 12.** Bias in ocean potential temperature (in K; top) and in salinity (in psu; bottom) with
 469 respect to EN4 (contours in all the panels; in K, top, and psu, bottom) in the a) VHR, b) HR, and
 470 c) LR models for the period 1980–2014. Stippling masks anomalies that are not significant at the
 471 5 % level. Each panel is separated into the upper and lower 500 m.
 472



473
 474 **Figure 13.** Mixed layer depth (in m) in the a) VHR, b) HR, and c) LR models for the period
 475 1980–2014. Northern Hemisphere and Southern Hemisphere values are for March and
 476 September, respectively.

477 Weak deep mixing results in a relatively weak Atlantic Meridional Overturning Circulation
 478 (AMOC; Fig. 14) in LR. The AMOC strength increases with resolution, related to the reduction
 479 of the cold bias and sea ice extent bias over the subpolar North Atlantic. The strength of the
 480 AMOC in VHR is thus the closest to the observed RAPID strength at 26 °N (17 ± 3 Sv,
 481 corresponding to the mean and standard deviation, respectively; Frajka-Williams et al., 2019)
 482 among the three models: 14 ± 3 Sv in VHR, 12 ± 4 Sv in HR, 11 ± 2 Sv in LR (computed from
 483 monthly streamfunction at 26 °N for the period 2004–2014). The structure of the AMOC cell is
 484 similar in the three model configurations, with a main positive cell in the upper 3000 m up to 60
 485 °N and with a maximum at around 30 °N, and a negative deeper one below with a strength of 2–
 486 4 Sv.



487 **Figure 14.** Atlantic overturning streamfunction (in Sv) in the a) VHR, b) HR, and c) LR models
 488 for the period 1980–2014.
 489

490 In HR, and even more in VHR, the cold bias over the Labrador Sea is replaced by a warm
491 bias (Fig. 4), up to 3–4 K in VHR. This bias also appears in other eddy-rich climate models,
492 related to a stronger ocean heat transport than at lower resolutions in the Atlantic (Roberts et al.,
493 2020b). Over the Nordic Seas, by contrast, a cold bias is present in the three models, although it
494 is somewhat reduced at VHR by 1–2 K compared to LR and HR (Fig. 4). In the three cases, this
495 bias is related to an excessively large sea ice cover in the region (Fig. 7). The warm bias over the
496 Labrador Sea and cold bias over the Nordic Seas in VHR might suggest a misrepresentation of
497 the distribution of oceanic heat transport between the two basins, favoring the westward transport
498 over the northward across-Ridge heat transport. It might also or instead be related to a
499 misrepresentation of the sea ice drift across the Denmark Strait (Gutjahr et al., 2022). Relatively
500 weak transport across the Strait would lead to ice deficit in the Labrador Sea, and hence
501 warming, and to ice accumulation in the Nordic Seas, hence cooling.

502 On a hemispheric scale, the three models simulate a slightly low Northern Hemisphere sea
503 ice extent, mainly due to the underestimation of the sea ice cover in the Sea of Okhotsk, Baltic
504 Sea, and Labrador Sea in HR and VHR (Fig. 8). By contrast, the three models show an overly
505 large sea ice volume by about 10^4 km³ compared to GIOMAS (Fig. 9), as they all simulate very
506 thick sea ice in the central Arctic (Fig. 7 for VHR). Anomalously thick ice in the central Arctic
507 would lead to an excess of brine rejection (not shown), which can explain the positive salinity
508 bias above 2 psu in the upper 100–200 m of the Arctic Ocean (Figs. 11 and 12). In VHR, the
509 associated increase in upper-ocean density leads to deeper oceanic mixing than in LR or HR,
510 with a mixed layer depth in the central Arctic that can reach up to 1000 m (Fig. 13).

511 Over the Pacific, biases tend to be weaker than over the Atlantic. A warm bias of about 1 K
512 develops over the subpolar North Pacific from LR to VHR (Fig. 4), which could explain the
513 negative bias in boreal winter (DJF) stormtrack aloft (Fig. 9) and the weaker jet stream over the
514 central Pacific in VHR (Fig. 10).

515 Over land, the cold bias over the Sahara is reduced with increased resolution (Fig. 4).
516 Similarly, the cold biases over large mountain ranges, such as the Rockies, the Andes, and the
517 Himalaya, up to about several degrees in LR are much reduced in VHR (Fig. 4), related to better
518 resolved orography.

519

520

521 **3.4. Southern Ocean**

522 The Southern Ocean is the region where VHR performs the worst compared to HR and LR. The
523 warm bias over the Southern Ocean increases with resolution, up to 4–5 K in VHR, compared to
524 1–2 K and 2–3 K for HR and LR respectively (Fig. 4). It tends to be largest over the Atlantic and
525 Indian sectors of the Southern Ocean and close to the Antarctic coast. Although the warm bias
526 remains generally confined to the upper 100–200 m at around 60 °S, it might also be connected
527 to the warm bias at depth between 2000 m and 4000 m (Fig. 12).

528 Two main mechanisms could explain the Southern Ocean warm bias: VHR has the largest
529 cloud cover underestimation of the three models, especially over the Atlantic and Indian sectors,
530 up to 15 % in VHR compared to 5–10 % in LR and HR (Fig. 5). Previous studies have related
531 the Southern Ocean warm biases to misrepresentation and underestimation of the mixed-phase
532 clouds, which lead to an excess of shortwave radiation reaching the surface, thereby warming it
533 (e.g., Hwang, and Frierson, 2013; Hyder et al., 2018). Connected to the warm bias, VHR also
534 shows the lowest sea ice extent of the three resolutions all year round (Figs. 7 and 8). Although
535 the three models underestimate the Antarctic sea ice extent, in VHR this is nearly half as in
536 observations for the same period (OSI SAF, 1980–2014). In terms of sea ice volume (Fig. 8),
537 however, LR shows larger values by about $2 \cdot 10^3 \text{ km}^3$ than GIOMAS between November and
538 April, pointing to overly thick sea ice. As for the extent, VHR also shows the lowest sea ice
539 volume, nearly half of the values in GIOMAS. The three models show the maximum volume one
540 month later than in GIOMAS, in October rather than in September. This contrasts with the
541 Arctic, where the three models capture the general shape of the seasonal cycle.

542 The surface warming over the Southern Ocean leads to a widespread underestimation of the
543 stormtracks (Fig. 9) and jet stream (Fig. 10) in the austral winter (JJA) in HR and, especially, in
544 VHR, compared to LR, which is much closer to ERA5. Although precipitation is also
545 underestimated over the Southern Ocean, specially in VHR, this is not a particularly strong bias,
546 at least compared to those over the tropical regions (Fig. 6).

547 Late austral summer (September) deep mixing tends to increase by about 200 m from LR to
548 HR and VHR, especially in the Pacific sector. These two latter resolutions show similar deep
549 mixing mean state, with variations only due to resolution and the better representation of the
550 mesoscale in VHR (Fig. 13). The underestimation of the stormtrack over the Southern Ocean
551 therefore does not seem to have an impact on the oceanic mixing below in VHR.

552 **3.5 Air–sea coupling**

553 We compare the change in the intensity of air–sea coupling from LR to VHR via the
554 computation of cross-correlation coefficients of the deseasonalized monthly SST and net surface
555 energy flux (Fig. 15). This analysis has extensively been used to study regions in which the
556 ocean tends to drive atmospheric variability (correlation coefficient values approaching one) or
557 vice versa (correlation coefficient values close to zero; e.g., Bishop et al., 2017; Small et al.,
558 2019). The three model configurations are compared with the ERA5 reanalysis, as done in the
559 previous sections for the biases. To complement the analysis with a non-model based product,
560 we also include satellite observations of radiative fluxes from J-OFURO3 (Tomita et al., 2019).
561 The two products show an overall good agreement, with areas of large correlation coefficient
562 values at the Equator, along the western boundary currents, and over the Southern Ocean (Fig.
563 15a,b). These areas, nonetheless, tend to be broader in J-OFURO3 than in ERA5.

564 Over the tropics, the three configurations tend to underestimate the coupling around the
565 Equator, although they all reproduce well the band of correlation coefficients of high values
566 along the equatorial Pacific and Atlantic. However, this band is narrower in LR and HR over the
567 subtropics than it is in ERA5 and J-OFURO3. VHR is thus the closest configuration to the two
568 reference observational products in the region. This result highlights the need for a model
569 resolution finer than 25 km in both the ocean and atmosphere to represent realistic tropical
570 climate interactions, in agreement with conclusions in Section 3.2.

571 At mid-latitudes, the coupling is greatly improved in HR and VHR compared to LR,
572 particularly over the subpolar regions compared to ERA5 and J-OFURO3. LR shows a rather
573 smooth pattern, with very low values in key regions over the Gulf Stream, Kuroshio Current, and
574 Southern Ocean, which suggests a standard 1° resolution is insufficient to represent a realistic
575 air–sea coupling. VHR and HR show, by contrast, sharper gradients in the correlation coefficient
576 values close to 1 over those regions. This result is consistent with previous studies, which also
577 found a degradation of the air–sea coupling in coarse grids, especially above 1° (e.g., Small et
578 al., 2019). However, VHR shows unrealistic broader areas of higher correlation coefficient
579 values than ERA5 and J-OFURO3 at mid-latitudes, degrading results from HR. One hypothesis
580 for this discrepancy might result from the difference of IFS grid resolution between VHR
581 (T1279) and ERA5 (T639), since the relationship between SST and turbulent fluxes shows
582 certain scale dependency (e.g., Small et al., 2019; Sun and Wu, 2022). However, results do not

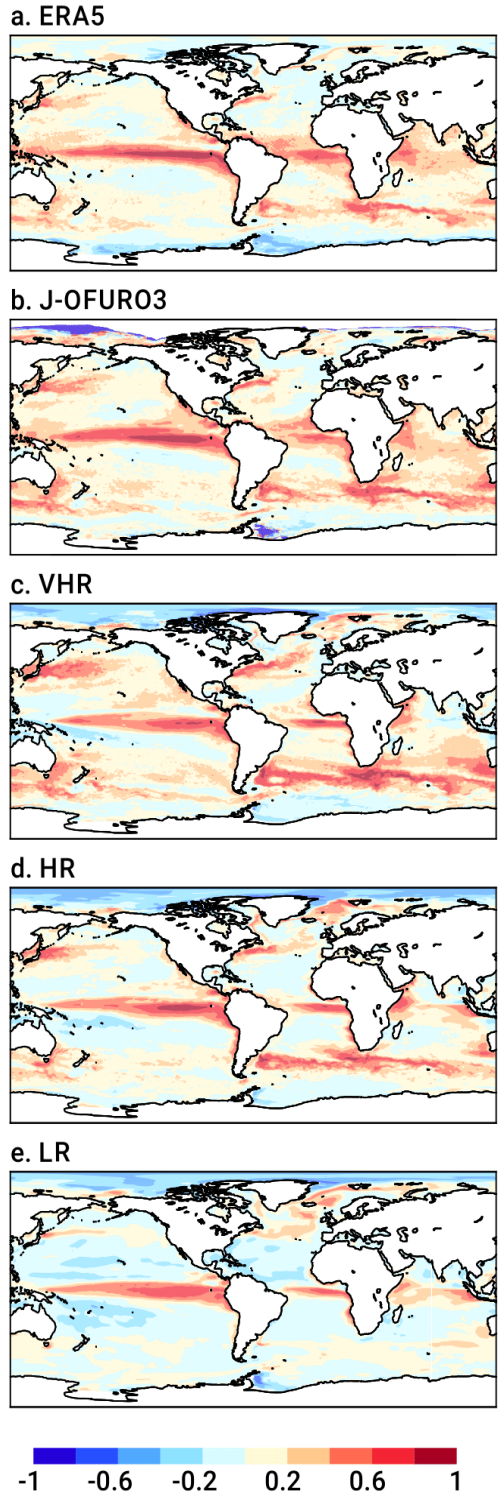
583 improve even when regridding VHR onto ERA5 grid before computing the correlation
584 coefficients (not shown). A second hypothesis is the lack of the ocean current feedback in VHR,
585 hence the lack of eddy-killing, which can control the simulated Gulf Stream's dynamics and
586 energy pathways (Renault et al., 2023). However, the pattern of correlation coefficient values
587 remains relatively unchanged when it is computed with a VHR configuration that includes a
588 parameterization that considers the wind adjustment to the ocean current feedback (not shown)
589 (Renault et al., 2019). The results suggest that the VHR's ocean exerts a stronger and more
590 widespread influence on the atmosphere variability than in HR and LR.

591 Further north, air–sea coupling is overestimated in all the models over the Nordic Seas, likely
592 related to the excess in sea ice in the region and its changes over the seasonal cycle. Together,
593 the results suggest that a realistic air–sea coupling requires grids finer than $1/4^\circ$ at least, with
594 potential local improvements on a $1/12^\circ$ grid, especially over the Tropics.

595

596 **4. Discussion and Conclusions**

597 This paper presents the eddy-rich configuration of the EC-Earth3P-VHR global model for
598 HighResMIP. We describe both the necessary technical developments to run the model
599 efficiently, and the main features of the simulated climate compared to recent observations
600 (1980–2014 period) and to two lower-resolution model configurations (the eddy-present, ~25-
601 km-grid EC-Earth3P-HR; and the non-eddy, ~100-km-grid EC-Earth3P-LR). The EC-Earth3P-
602 VHR (or VHR) uses a comparable atmospheric and oceanic resolution of 10–15 km in a global
603 fully coupled setup, which is, to our knowledge, one of the finest combined grids ever used to
604 date to perform long climate integrations for CMIP (e.g., Small et al., 2014, Chang et al., 2020).
605 Our focus here is on the HighResMIP historical simulation (HighResMIP's hist-1950). This run
606 is part of a larger set of runs, which includes a spin-up and control runs (HighResMIP's control-
607 1950), a future extension under the ssp8.5 scenario (HighResMIP's highres-future), three hosing
608 simulations forced by idealized Greenland melting, and AMIP sensitivity simulations, all
609 performed within the European PRIMAVERA project and the Spanish STREAM project. Those
610 additional simulations will be described in their corresponding publications, which are currently
611 in preparation.



612
 613 **Figure 15.** Cross-correlation coefficients between monthly SST and net surface energy flux for
 614 the period 1980–2014 in a) ERA5, b) J-OFURO3, and in the c) VHR, d) HR, and e) LR models.
 615 The seasonal cycle and linear trends are removed from the monthly SSTs and energy fluxes
 616 before the correlation coefficients are computed. This is done on the original grid in all the cases.

617 The comparison across the three resolutions (this is, VHR, HR, and LR), all with the same
618 physics and no additional tuning, allows identifying regions where increased resolution improves
619 the model performance with respect to observations. One of those regions is the Tropics, and
620 specially the equatorial Pacific, where the cold tongue bias and the dry bias above are both
621 reduced in VHR compared to HR and LR. Wengel et al. (2021) also reports a similar bias
622 reduction in an eddy-resolving configuration of the CESM (0.25° resolution in the atmosphere,
623 0.1° resolution in the ocean), which they link to better represented mesoscale features, such as
624 tropical instability waves. Similarly, the HadGEM3-GC3.1 global model shows a reduced dry
625 bias over the equatorial Pacific in its configuration with a 1/12° ocean and a 50-km atmosphere
626 (Roberts et al., 2019). By contrast, the eddy-rich MPI-ESM1.2-ER global model (1/12° ocean as
627 well) shows no evident changes in equatorial precipitation when coupled to a 100-km
628 atmosphere (Gutjahr et al., 2019). Combined, these results suggest that resolutions finer than 25–
629 50 km might be needed in both the atmosphere and ocean to improve surface coupling and
630 reduce biases. However, minimizing equatorial precipitation biases might actually be much more
631 complex than simply increasing model resolution, as found for the ICON global atmosphere–
632 ocean model with a uniform grid spacing of 5 km. Despite its high atmosphere and ocean
633 resolutions, this model still exhibits a strong dry bias over the equatorial Pacific driven by a
634 surface cold bias underneath (Hohenegger et al., 2023; Segura et al., 2022). This model,
635 however, is not directly comparable to those other HighResMIP models, as it includes a
636 minimum set of parametrization. Thus, while convection is directly resolved in ICON, it is
637 parametrized in VHR and the listed models. The incorrect representation of the equatorial SST
638 structure in ICON might instead be related to unresolved sub-grid processes (Segura et al.,
639 2022).

640 The Gulf Stream is another region in which increased model resolution is beneficial, with a
641 reduced temperature biases over the separation region and the central North Atlantic in VHR
642 compared to HR and LR. Such improvements have been related to the resolving of the first
643 baroclinic Rossby radius of deformation over most of the region and/or the exceeding of a
644 critical Reynolds number (e.g., Chassignet and Marshall, 2008) and have been linked to the
645 increase in resolution over the shelf areas to the north of the Gulf Stream (Sein et al., 2017).
646 Similar results have also been reported for the HadGEM3-GC3.1 (Roberts et al., 2019) and MPI-
647 ESM1.2-ER (Gutjahr et al., 2019) global models, both with a 1/12° oceanic grid but coarser

648 atmospheric grids (~50 km and ~100 km, respectively). This suggests that oceanic resolution is a
649 critical factor for the Gulf Stream representation. Nonetheless, other model features might also
650 be relevant to simulate a realistic Gulf Stream, as no improvement is found in the CESM1.3
651 model between a 1°- and a 0.1°- oceanic grid, for which the Gulf Stream separation occurs too
652 far north (Chang et al., 2020). One of the many potential reasons behind the discrepancy might
653 be the obvious difference in the number of atmospheric vertical levels: 91 in VHR, 85 in
654 HadGEM3-GC3.1 (Roberts et al., 2019), 95 in MPI-ESM1.2-ER (Gutjahr et al., 2019), but only
655 30 in CESM1.3 (Meehl et al., 2019), which is expected to degrade the representation of key
656 stratosphere–troposphere interactions affecting North Atlantic variability, and, by extension, the
657 wind field, which is critical for the Gulf Stream separation. As nicely summarized in Chassignet
658 and Marshall (2008), however: “The Gulf Stream separation, indeed, turns out to be quite
659 sensitive to a variety of other factors such as subgrid scale parametrization, subpolar gyre
660 strength and water mass properties, [deep western boundary current] strength, representation of
661 topography, and the choice of model grid”. A realistic representation of the Gulf Stream is
662 crucial for the North Atlantic and European climate. SST biases in the Gulf Stream can drive not
663 only local changes over the North Atlantic, but a large-scale dynamic response over remote
664 regions of the Northern Hemisphere through a quasi-zonal planetary barotropic Rossby wave
665 response (Lee et al., 2018). Similarly, a more realistic, farther-south Gulf Stream has been shown
666 to shift north in simulations with increased CO₂ in models at eddy-rich resolutions (Saba et al.,
667 2016; Moreno-Chamarro et al., 2021). This shift would lead to amplified warming of the US East
668 coastal region, which might be consistent with the anomalous warming observed in the Gulf
669 Stream area in recent decades (Pershing et al., 2015; Todd and Ren, 2023). Reducing biases in
670 the Gulf Stream area is therefore key to reproducing a realistic atmospheric circulation and to the
671 sensitivity of the response to an external forcing.

672 Mainly related to increased atmospheric resolution, VHR also shows reduced precipitation
673 biases over mountain ranges all over the world. This suggests VHR might provide more realistic
674 regional information of precipitation variability and future changes than lower resolution models
675 can. Giorgi et al. (2016), in fact, showed that increased model resolution leads to stronger
676 summer precipitation changes over the Alpine region, using climate change projections with a
677 regional atmospheric model of ~12-km grid. VHR uses a similar resolution but on a global scale,
678 without the need to be constrained by lower resolution models.

679 On the negative side, we find that increased model resolution alone can be insufficient to
680 reduce important and well-known biases in the climate or even cause model degradation in VHR.
681 The warm bias over the coastal tropical upwelling areas, the Southern Ocean warm bias, and the
682 rainfall excess bias over warm tropical waters all persist or even increase in VHR compared to
683 HR and LR. These biases point to deficiencies in the model physics, specially in the atmosphere,
684 and more particularly, in the cloud parameterizations. In VHR, both the warm bias over eastern
685 tropical upwelling areas and the Southern Ocean are connected to negative biases in cloud cover.
686 This reinforces the established idea that insufficient stratocumulus decks over the upwelling
687 areas (e.g., Richter, 2015) and mixed-phase clouds over the Southern Ocean (e.g., Hyder et al.,
688 2018) play key roles in setting up those bias. Cloud biases can be particularly insensitive to
689 increases in model resolution, both in the ocean and atmosphere, from ~100-km grids to 25–50-
690 km grids (Moreno-Chamarro et al., 2022). Yet, for example, improved cloud microphysics closer
691 to observations have been shown to help reduce shortwave radiation biases over the Southern
692 Ocean in the Met Office's Unified Model (Varma et al., 2020). Reducing these biases as much as
693 possible is critical, since they can have wider, global impacts on the climate, driving, for
694 example, additional biases in tropical precipitation through the effect on the global energy budget
695 (e.g., Hwang et al., 2013; Hawcroft et al., 2017).

696 It is interesting to note, nonetheless, that although LR, HR, and VHR all share the same cloud
697 scheme, it is VHR that develops the strongest Southern Ocean bias. This might be related to the
698 lack of additional model tuning from LR to HR and VHR. Rackow et al. (2024) showed that
699 tuning the top-of-the-atmosphere radiation contributed to reducing the warming excess over the
700 Southern Ocean in the IFS-FESOM global model at ~5-km resolution. The HighResMIP
701 protocol suggests that no tuning is performed across resolutions to ensure any changes in the
702 simulated climate can solely be attributed to changes in resolution (Haarsma et al., 2016). This
703 approach can lead to undesired model degradation: for example, the untuned, low-resolution
704 ECMWF model for HighResMIP shows an overly weak AMOC and a large cold bias over the
705 North Atlantic compared to its well-tuned, high-resolution counterpart (Roberts C.D. et al.,
706 2018). This can hinder model comparison and a clean understanding of the effect of model
707 resolution, as biases can have large-scale climatic impacts (e.g., Hwang et al., 2013; Hawcroft et
708 al., 2017; Lee et al., 2018) and affect the response sensitivity to forcing (e.g., McGee et al.,
709 2018).

710 With respect to the spin-up, the HighResMIP protocol suggests a 50-year period (Haarsma et
711 al., 2016). For all the configurations, this period is insufficient to equilibrate the full ocean,
712 although the upper 100 m equilibrates faster than the lower-part, and VHR does it faster and
713 appears more stable after 100 years than HR and LR. The eddy-rich HadGEM3-GC3.1 also
714 shows smaller drifts at the end of the 50-year period than its lowest resolution versions (Roberts
715 et al., 2019). By contrast, for the CESM1.3 model, the low and high-resolution configurations
716 only show a more stable climate after 150 years, related to a strong top-of-the-atmosphere energy
717 imbalance (Chang et al., 2020). This led the authors to propose “150 to 200 years of model spin-
718 up as a future strategy for initializing HR climate model simulations” (Chang et al., 2020).
719 However, considering how computationally expensive these simulations are, new techniques
720 might need to be introduced to tune and spin these models up faster and for longer. As much as
721 tuning can still be “artisanal in character” at many research centers (Mauritsen et al., 2012), new
722 and faster methods are being implemented to speed up the exploration of the space of parameters
723 to find the best fit with observations. These methods include for example machine learning
724 (Hourdin et al., 2021), simplified configurations (Wan et al., 2014) , adjoints (Lyu et al., 2018),
725 or model emulators (Williamson et al., 2013). Additional techniques have also been proposed to
726 spin models up faster at much less computational costs; these include using for example Newton-
727 Krylov methods (Bernsen et al., 2008; Merlis and Khatiwala, 2008), or replacing the atmosphere
728 model by model data (Lofverstrom et al., 2020). Implementing similar techniques in future HR
729 and VHR simulations would help accelerate both the spin-up and tuning phases.

730 To summarize, we here present the eddy-rich version of the EC-Earth global climate model,
731 EC-Earth3P-VHR, with atmospheric and oceanic resolutions of 10–15 km. The analysis of its
732 main climate features reveals improvements with respect to two lower resolution versions, such
733 as a reduced dry equatorial bias over the Pacific, a more realistic Gulf Stream representation, and
734 more accurate rainfall over mountain areas. Other biases persist or degrade, such as the warm
735 biases over the subtropical upwelling regions and Southern Ocean, the tropical precipitation
736 excess, or the excess in sea ice volume and oceanic deep mixing in the Arctic. VHR's global
737 resolution is at a similar level of many regional models, such as those participating in CORDEX,
738 and it is much finer than most of the standard CMIP models. This opens a window of opportunity
739 for model comparison and evaluation, as well as process understanding of much more realistic
740 present-day and future climate and on a more regional scale.

741

742 **Code and Data Availability**

743 The data of the EC-Earth3P-LR and -HR models are available from ESGF ([https://esgf-](https://esgf-index1.ceda.ac.uk/search/cmip6-ceda/)
744 [index1.ceda.ac.uk/search/cmip6-ceda/](https://esgf-index1.ceda.ac.uk/search/cmip6-ceda/), last access: 20 June 2024) via the references provided in
745 Section 2.3: EC-Earth3P (<https://doi.org/10.22033/ESGF/CMIP6.4683>, EC-Earth, 2018;
746 <https://doi.org/10.22033/ESGF/CMIP6.4682>, EC-Earth, 2019). Data of ERA-5 are freely
747 available at <https://www.ecmwf.int/en/forecasts/dataset/ecmwf-reanalysis-v5> (Hersbach et al.,
748 2020; <https://doi.org/10.24381/cds.6860a573>, Hersbach et al., 2019), while GPCP data are at
749 <https://psl.noaa.gov/data/gridded/data.gpcp.html> (Adler et al., 2003), ESA cloud cover data are at
750 <https://climate.esa.int/en/projects/cloud/data/> (Stengel et al., 2020), EN4 data version 4.2.2 are at
751 <https://www.metoffice.gov.uk/hadobs/en4/> (Good et al., 2013), OSI SAF (OSI-409/OSI-409-a)
752 sea ice concentration data are at <https://osi-saf.eumetsat.int/products/sea-ice-products>
753 (EUMETSAT Ocean and Sea Ice Satellite Application Facility, 2015), GIOMAS sea ice volume
754 data are at https://psc.apl.washington.edu/zhang/Global_seaice/data.html (Zhang and Rothrock,
755 2003), and J-OFURO3 flux data are at <https://www.j-ofuro.com/en/dataset/> (Tomita et al., 2019).
756 The model data and plot scripts to reproduce the figures can be obtained from
757 <https://zenodo.org/records/12078052> (Moreno-Chamarro, 2024). The model code developed at
758 ECMWF, including IFS and the Finite Volume Module (FVM), is intellectual property of
759 ECMWF and its member states. Permission to access the EC-Earth source code can be requested
760 from the EC-Earth community via the EC-Earth website (<http://www.ec-earth.org/>, last access:
761 July 2024) and may be granted, if a corresponding software license agreement is signed with
762 ECMWF. The repository tag for the version of IFS and EC-Earth3P-VHR used in this work is
763 3.2.2 (see Section 2.1) and is available through r8643. The EC-Earth workflow software used to
764 run the simulations at the BSC, Auto-EC-Earth, is stored and version controlled in the BSC Earth
765 Sciences GitLab repository (<https://earth.bsc.es/gitlab/es/auto-ecearth3>, last access: July 2024).
766 Permission to access the repository can be requested from the Earth Sciences Department at the
767 BSC and may be granted, if the applicant has access to the EC-Earth code and the BSC HPC
768 infrastructure. The workflow management system for running the simulations is distributed
769 under Apache License 2.0 as a public project (<https://earth.bsc.es/gitlab/es/autosubmit>, last
770 access: July 2024) in the BSC GitLab repository.

771

772 **Author Contributions**

773 TA, MA, MC, EF, and SP developed the model setup. EMC and TA ran the simulations. PAB
774 and DK post-processed and comorized the model data. EMC analyzed the data and wrote the
775 manuscript with input from all the authors.

776

777 **Competing interests**

778 The authors declare that they have no conflict of interest.

779

780 **Acknowledgements**

781 This research has been supported by the Horizon2020 PRIMAVERA project (H2020 GA
782 641727). EMC acknowledges funding from the Spanish Science and Innovation Ministry
783 (Ministerio de Ciencia e Innovación) via the STREAM project (PID2020-114746GB-I00). MA
784 has received funding from the National Research Agency through OEMES (PID2020-
785 116324RA-I00). This work has received funding from the European High Performance
786 Computing Joint Undertaking (JU) under the ESiWACE CoE, grant agreement No 101093054.

787

788 **References**

789 Abdalla, S., Isaksen, L., Janssen, P. A. E. M., and Nils, W.: Effective spectral resolution of
790 ECMWF atmospheric forecast models, ECMWF Newsletter No. 137, 19–22,
791 <https://doi.org/10.21957/rue4o7ac>, 2013.

792 Acosta, M.C., Palomas, S. and Tourigny, E.: Balancing EC-Earth3 Improving the
793 Performance of EC-Earth CMIP6 Configurations by Minimizing the Coupling Cost. *Earth
794 and Space Science*, 10(8), p.e2023EA002912, <https://doi.org/10.1029/2023EA002912>,
795 2023.

796 Acosta, M. C., Palomas, S., Paronuzzi Ticco, S. V., Utrera, G., Biercamp, J., Bretonniere, P.-
797 A., Budich, R., Castrillo, M., Caubel, A., Doblás-Reyes, F., Epicoco, I., Fladrich, U.,
798 Joussaume, S., Kumar Gupta, A., Lawrence, B., Le Sager, P., Lister, G., Moine, M.-P.,
799 Rioual, J.-C., Valcke, S., Zadeh, N., and Balaji, V.: The computational and energy cost of
800 simulation and storage for climate science: lessons from CMIP6, *Geosci. Model Dev.*, 17,
801 3081–3098, <https://doi.org/10.5194/gmd-17-3081-2024>, 2024.

802 Adler, R. F., Huffman, G. J., Chang, A., Ferraro, R., Xie, P. P., Janowiak, J., Rudolf, B.,
803 Schneider, U., Curtis, S., Bolvin, D., and Gruber, A.: The version-2 global precipitation
804 climatology project (GPCP) monthly precipitation analysis (1979–present), *J.*
805 *Hydrometeorol.*, 4, 1147–1167, [https://doi.org/10.1175/1525-](https://doi.org/10.1175/1525-7541(2003)004<1147:TVGPCP>2.0.CO;2)
806 [7541\(2003\)004<1147:TVGPCP>2.0.CO;2](https://doi.org/10.1175/1525-7541(2003)004<1147:TVGPCP>2.0.CO;2), 2003 (data available at:
807 <https://psl.noaa.gov/data/gridded/data.gpcp.html>, last access: 30 March 2023).

808 Amante, C. and Eakins, B.W.: ETOPO1 arc-minute global relief model: procedures, data
809 sources and analysis, 2009.

810 Baker, A.J., Schiemann, R., Hodges, K.I., Demory, M. E., Mizielinski, M. S., Roberts, M. J.,
811 Shaffrey, L. C., Strachan, J. and Vidale, P. L.: Enhanced climate change response of
812 wintertime North Atlantic circulation, cyclonic activity, and precipitation in a 25-km-
813 resolution global atmospheric model. *Journal of Climate*, 32(22), 7763–7781,
814 <https://doi.org/10.1175/JCLI-D-19-0054.1>, 2019.

815 Balsamo, G., Beljaars, A., Scipal, K., Viterbo, P., van den Hurk, B., Hirschi, M., and Betts, A.
816 K.: A revised hydrology for the ECMWF model: Verification from field site to terrestrial
817 water storage and impact in the Integrated Forecast System, *J. Hydrometeorol.*, 10, 623–643,
818 2009.

819 Becker, J.J., Sandwell, D.T., Smith, W.H.F., Braud, J., Binder, B., Depner, J.L., Fabre, D.,
820 Factor, J., Ingalls, S., Kim, S.H. and Ladner, R.: Global bathymetry and elevation data at 30
821 arc seconds resolution: SRTM30_PLUS. *Marine Geodesy*, 32(4), 355–371,
822 <https://doi.org/10.1080/01490410903297766>, 2009.

823 Bellucci, A., Athanasiadis, P. J., Scoccimarro, E., Ruggieri, P., Gualdi, S., Fedele, G.,
824 Haarsma, R. J., Garcia-Serrano, J., Castrillo, M., Putrahasan, D., and Sanchez-Gomez, E.:
825 Air-Sea interaction over the Gulf Stream in an ensemble of HighResMIP present climate
826 simulations, *Clim. Dynam.*, 56, 2093–2111, <https://doi.org/10.1007/s00382-020-05573-z>,
827 2021.

828 Bernsen, E., Dijkstra, H.A., Thies, J. and Wubs, F.W.: The application of Jacobian-free
829 Newton–Krylov methods to reduce the spin-up time of ocean general circulation models.
830 *Journal of Computational Physics*, 229(21), 8167–8179,
831 <https://doi.org/10.1016/j.jcp.2010.07.015>, 2010.

832 Biastoch, A., Schwarzkopf, F. U., Getzlaff, K., Rühls, S., Martin, T., Scheinert, M., Schulzki,
833 T., Handmann, P., Hummels, R. and Böning, C. W.: Regional imprints of changes in the
834 Atlantic Meridional Overturning Circulation in the eddy-rich ocean model VIKING20X.
835 *Ocean Science*, 17(5), 1177–1211, <https://doi.org/10.5194/os-17-1177-2021>, 2021.

836 Bishop, S. P., Small, R. J., Bryan, F. O. and Tomas, R. A.: Scale dependence of midlatitude
837 air–sea interaction. *Journal of Climate*, 30(20), 8207–8221, [https://doi.org/10.1175/JCLI-D-](https://doi.org/10.1175/JCLI-D-17-0159.1)
838 [17-0159.1](https://doi.org/10.1175/JCLI-D-17-0159.1), 2017.

839 Chang, P., Zhang, S., Danabasoglu, G., Yeager, S.G., Fu, H., Wang, H., Castruccio, F.S.,
840 Chen, Y., Edwards, J., Fu, D. and Jia, Y.: An unprecedented set of high-resolution earth
841 system simulations for understanding multiscale interactions in climate variability and
842 change. *Journal of Advances in Modeling Earth Systems*, 12(12), e2020MS002298,
843 <https://doi.org/10.1029/2020MS002298>, 2020.

844 Chassignet, E. and Marshall, D.: Gulf Stream separation in numerical ocean models.
845 *Geophysical Monograph Series*, 177, <https://doi.org/10.1029/177GM05>, 2008.

846 Craig, A., Valcke, S., and Coquart, L.: Development and performance of a new version of the
847 OASIS coupler, OASIS3-MCT_3.0, *Geosci. Model Dev.*, 10, 3297–3308,
848 <https://doi.org/10.5194/gmd-10-3297-2017>, 2017.

849 Czaja, A., Frankignoul, C., Minobe, S. and Vanni re, B.: Simulating the midlatitude
850 atmospheric circulation: what might we gain from high-resolution modeling of air-sea
851 interactions?. *Current climate change reports*, 5, 390–406, [https://doi.org/10.1007/s40641-](https://doi.org/10.1007/s40641-019-00148-5)
852 [019-00148-5](https://doi.org/10.1007/s40641-019-00148-5), 2019.

853 Doi, T., Vecchi, G. A., Rosati, A. J., and Delworth, T. L.: Biases in the Atlantic ITCZ in
854 seasonal–interannual variations for a coarse-and a high-resolution coupled climate model, *J.*
855 *Climate*, 25, 5494–5511, <https://doi.org/10.1175/JCLI-D-11-00360.1>, 2012.

856 D scher, R., Acosta, M., Alessandri, A., Anthoni, P., Arsouze, T., Bergman, T., Bernardello,
857 R., Boussetta, S., Caron, L.-P., Carver, G., Castrillo, M., Catalano, F., Cvijanovic, I.,
858 Davini, P., Dekker, E., Doblas-Reyes, F. J., Docquier, D., Echevarria, P., Fladrich, U.,
859 Fuentes-Franco, R., Gr ger, M., v. Hardenberg, J., Hieronymus, J., Karami, M. P.,
860 Keskinen, J.-P., Koenigk, T., Makkonen, R., Massonnet, F., M n goz, M., Miller, P. A.,
861 Moreno-Chamarro, E., Nieradzick, L., van Noije, T., Nolan, P., O'Donnell, D., Ollinaho, P.,
862 van den Oord, G., Ortega, P., Prims, O. T., Ramos, A., Reerink, T., Rousset, C., Ruprich-

863 Robert, Y., Le Sager, P., Schmith, T., Schrödner, R., Serva, F., Sicardi, V., Sloth Madsen,
864 M., Smith, B., Tian, T., Tourigny, E., Uotila, P., Vancoppenolle, M., Wang, S., Wårlind, D.,
865 Willén, U., Wyser, K., Yang, S., Yepes-Arbós, X., and Zhang, Q.: The EC-Earth3 Earth
866 system model for the Coupled Model Intercomparison Project 6, *Geosci. Model Dev.*, 15,
867 2973–3020, <https://doi.org/10.5194/gmd-15-2973-2022>, 2022.

868 EC-Earth Consortium (EC-Earth): EC-Earth-Consortium EC-Earth3P-HR model output
869 prepared for CMIP6 HighResMIP hist-1950, Earth System Grid Federation [data set; last
870 access: 18 May 2023], <https://doi.org/10.22033/ESGF/CMIP6.4683>, 2018.

871 EC-Earth Consortium (EC-Earth): EC-Earth-Consortium EC-Earth3P model output prepared
872 for CMIP6 HighResMIP hist-1950, Earth System Grid Federation [data set; last access: 18
873 May 2023], <https://doi.org/10.22033/ESGF/CMIP6.4682>, 2019.

874 EUMETSAT Ocean and Sea Ice Satellite Application Facility: Global sea ice concentration
875 reprocessing dataset 1978–2015 (v1.2), Norwegian and Danish Meteorological Institutes,
876 available at: <https://catalogue.ceda.ac.uk/uuid/8bbde1a8a0ce4a86904a3d7b2b917955> (last
877 access: 8 February 2019), 2015.

878 Frajka-Williams, E., Ansorge, I.J., Baehr, J., Bryden, H.L., Chidichimo, M.P., Cunningham,
879 S.A., Danabasoglu, G., Dong, S., Donohue, K.A., Elipot, S. Heimbach, P., Holliday, N.P.,
880 Hummels, R., Jackson, L.C., Karstensen, J., Lankhorst, M., Le Bras, I.A., Lozier, M. S.,
881 McDonagh, E.L., Meinen, C.S., Mercier, H., Moat, B.I., Perez, R.C., Piecuch, C.G., Rhein,
882 M., Srokosz, M.A., Trenberth, K.E., Bacon, S., Forget, G., Goni, G., Kieke, D., Koelling, J.,
883 Lamont, T., McCarthy, G.D., Mertens, C., Send, U., Smeed, D.A., Speich, S., van den Berg,
884 M., Volkov, D., Wilson, C.: Atlantic Meridional Overturning Circulation: Observed
885 Transport and Variability, *Frontiers in Marine Science*, 6,
886 <https://doi.org/10.3389/fmars.2019.00260>, 2019.

887 Giorgi, F., Torma, C., Coppola, E., Ban, N., Schär, C. and Somot, S.: Enhanced summer
888 convective rainfall at Alpine high elevations in response to climate warming. *Nature*
889 *Geoscience*, 9(8), 584-589, <https://doi.org/10.1038/ngeo2761>, 2016.

890 Good, S. A., M. J. Martin, M. J., and Rayner, N. A.: EN4: quality controlled ocean
891 temperature and salinity profiles and monthly objective analyses with uncertainty estimates,
892 *Journal of Geophysical Research: Oceans*, 118, 6704-6716,

893 <https://doi.org/10.1002/2013JC009067>, 2013 (data available at:
894 <https://www.metoffice.gov.uk/hadobs/en4/>, last access: 12 November 2021).

895 Gutjahr, O., Jungclaus, J. H., Brüggemann, N., Haak, H. and Marotzke, J.: Air-sea
896 interactions and water mass transformation during a katabatic storm in the Irminger sea.
897 *Journal of Geophysical Research: Oceans*, 127(5),
898 e2021JC018075, <https://doi.org/10.1029/2021JC018075>, 2022.

899 Gutjahr, O., Putrasahan, D., Lohmann, K., Jungclaus, J.H., von Storch, J.S., Brüggemann, N.,
900 Haak, H. and Stössel, A.: Max Planck Institute earth system model (MPI-ESM1.2) for the
901 high-resolution model intercomparison project (HighResMIP). *Geoscientific Model*
902 *Development*, 12(7), 3241–3281, <https://doi.org/10.5194/gmd-12-3241-2019>, 2019.

903 Haarsma, R., Acosta, M., Bakhshi, R., Bretonnière, P. A., Caron, L. P., Castrillo, M., Corti,
904 S., Davini, P., Exarchou, E., Fabiano, F. and Fladrich, U.: HighResMIP versions of EC-
905 Earth: EC-Earth3P and EC-Earth3P-HR—description, model computational performance and
906 basic validation. *Geoscientific Model Development*, 13(8), 3507–3527,
907 <https://doi.org/10.5194/gmd-13-3507-2020>, 2020.

908 Haarsma, R. J., Roberts, M. J., Vidale, P. L., Senior, C. A., Bellucci, A., Bao, Q., Chang, P.,
909 Corti, S., Fučkar, N. S., Guemas, V., von Hardenberg, J., Hazeleger, W., Kodama, C.,
910 Koenigk, T., Leung, L. R., Lu, J., Luo, J.-J., Mao, J., Mizielinski, M. S., Mizuta, R., Nobre,
911 P., Satoh, M., Scoccimarro, E., Semmler, T., Small, J., and von Storch, J.-S.: High
912 Resolution Model Intercomparison Project (HighResMIP v1.0) for CMIP6, *Geosci. Model*
913 *Dev.*, 9, 4185–4208, <https://doi.org/10.5194/gmd-9-4185-2016>, 2016.

914 Haarsma, R., Acosta, M., Bakhshi, R., Bretonnière, P.-A., Caron, L.-P., Castrillo, M., Corti,
915 S., Davini, P., Exarchou, E., Fabiano, F., Fladrich, U., Fuentes Franco, R., García-Serrano,
916 J., von Hardenberg, J., Koenigk, T., Levine, X., Meccia, V. L., van Noije, T., van den Oord,
917 G., Palmeiro, F. M., Rodrigo, M., Ruprich-Robert, Y., Le Sager, P., Tourigny, E., Wang, S.,
918 van Weele, M., and Wyser, K.: HighResMIP versions of EC-Earth: EC-Earth3P and EC-
919 Earth3P-HR – description, model computational performance and basic validation, *Geosci.*
920 *Model Dev.*, 13, 3507–3527, <https://doi.org/10.5194/gmd-13-3507-2020>, 2020.

921 Hawcroft, M., Haywood, J.M., Collins, M., Jones, A., Jones, A.C. and Stephens, G., 2017.
922 Southern Ocean albedo, inter-hemispheric energy transports and the double ITCZ: Global

923 impacts of biases in a coupled model. *Climate Dynamics*, 48, 2279–2295,
924 <https://doi.org/10.1007/s00382-016-3205-5>, 2017.

925 Hazeleger, W., Wang, X., Severijns, C., Ştefănescu, S., Bintanja, R., Sterl, A., Wyser, K.,
926 Semmler, T., Yang, S., van den Hurk, B., van Noije, T., van der Linden, E., and van der
927 Wiel, K.: EC-Earth V2.2: description and validation of a new seamless earth system
928 prediction model, *Clim. Dynam.*, 39, 2611–2629, 2012.

929 Hewitt, H. T., Bell, M. J., Chassignet, E. P., Czaja, A., Ferreira, D., Griffies, S. M., Hyder, P.,
930 McClean, J. L., New, A. L., and Roberts, M. J.: Will high-resolution global ocean models
931 benefit coupled predictions on short-range to climate timescales?, *Ocean Model.*, 120, 120–
932 136, <https://doi.org/10.1016/j.ocemod.2017.11.002>, 2017.

933 Hersbach, H., Bell, B., Berrisford, P., Biavati, G., Horányi, A., Muñoz Sabater, J., Nicolas, J.,
934 Peubey, C., Radu, R., Rozum, I., Schepers, D., Simmons, A., Soci, C., Dee, D., and
935 Thépaut, J.-N.: ERA5 monthly averaged data on pressure levels from 1979 to present,
936 Copernicus Climate Change Service (C3S) Climate Data Store (CDS) [data set],
937 <https://doi.org/10.24381/cds.6860a573>, 2019.

938 Hersbach, H., Bell, B., Berrisford, P., Hirahara, S., Horányi, A., Muñoz-Sabater, J., Nicolas,
939 J., Peubey, C., Radu, R., Schepers, D., Simmons, A., Soci, C., Abdalla, S., Abellan, X.,
940 Balsamo, G., Bechtold, P., Biavati, G., Bidlot, J., Bonavita, M., Chiara, G. D., Dahlgren, P.,
941 Dee, D., Diamantakis, M., Dragani, R., Flemming, J., Forbes, R., Fuentes, M., Geer, A.,
942 Haimberger, L., Healy, S., Hogan, R. J., Hólm, E., Janisková, M., Keeley, S., Laloyaux, P.,
943 Lopez, P., Lupu, C., Radnoti, G., de Rosnay, P., Rozum, I., Vamborg, F., Villaume, S., and
944 Thépaut, J.: The ERA5 global reanalysis, *Q. J. Roy. Meteor. Soc.*, 146, 1999–2049,
945 <https://doi.org/10.1002/qj.3803>, 2020 (data available at:
946 <https://www.ecmwf.int/en/forecasts/dataset/ecmwf-reanalysis-v5>, last access: 23 January
947 2020).

948 Hodges, K. I., Lee, R. W., and Bengtsson, L.: A comparison of extratropical cyclones in
949 recent reanalyses ERA-Interim, NASA MERRA, NCEP CFSR, and JRA-25, *J. Climate*, 24,
950 4888–4906, <https://doi.org/10.1175/2011JCLI4097.1>, 2011.

951 Hoffmann, J., Bauer, P., Sandu, I., Wedi, N., Geenen, T. and Thiemert, D.: Destination Earth–
952 A digital twin in support of climate services. *Climate Services*, 30, 100394,
953 <https://doi.org/10.1016/j.cliser.2023.100394>, 2023.

954 Hohenegger, C., Korn, P., Linardakis, L., Redler, R., Schnur, R., Adamidis, P., Bao, J.,
955 Bastin, S., Behraves, M., Bergemann, M., Biercamp, J., Bockelmann, H., Brokopf, R.,
956 Brüggemann, N., Casaroli, L., Chegini, F., Datsaris, G., Esch, M., George, G., Giorgetta,
957 M., Gutjahr, O., Haak, H., Hanke, M., Ilyina, T., Jahns, T., Jungclaus, J., Kern, M., Klocke,
958 D., Kluft, L., Kölling, T., Kornbluh, L., Kosukhin, S., Kroll, C., Lee, J., Mauritsen, T.,
959 Mehlmann, C., Mieslinger, T., Naumann, A. K., Paccini, L., Peinado, A., Praturi, D. S.,
960 Putrasahan, D., Rast, S., Riddick, T., Roeber, N., Schmidt, H., Schulzweida, U., Schütte, F.,
961 Segura, H., Shevchenko, R., Singh, V., Specht, M., Stephan, C. C., von Storch, J.-S., Vogel,
962 R., Wengel, C., Winkler, M., Ziemann, F., Marotzke, J., and Stevens, B.: ICON-Sapphire:
963 simulating the components of the Earth system and their interactions at kilometer and
964 subkilometer scales, *Geosci. Model Dev.*, 16, 779–811, [https://doi.org/10.5194/gmd-16-](https://doi.org/10.5194/gmd-16-779-2023)
965 [779-2023](https://doi.org/10.5194/gmd-16-779-2023), 2023.

966 Hourdin, F., Williamson, D., Rio, C., Couvreur, F., Roebrig, R., Villefranque, N., Musat, I.,
967 Fairhead, L., Diallo, F. B. and Volodina, V.: Process-based climate model development
968 harnessing machine learning: II. Model calibration from single column to global. *Journal of*
969 *Advances in Modeling Earth Systems*, 13(6), e2020MS002225,
970 <https://doi.org/10.1029/2020MS002225>, 2021.

971 Hwang, Y. T. and Frierson, D. M.: Link between the double-Intertropical Convergence Zone
972 problem and cloud biases over the Southern Ocean, *P. Natl. Acad. Sci. USA*, 110, 4935–
973 4940, <https://doi.org/10.1073/pnas.1213302110>, 2013.

974 Hyder, P., Edwards, J. M., Allan, R. P., Hewitt, H. T., Bracegirdle, T. J., Gregory, J. M.,
975 Wood, R. A., Meijers, A. J., Mulcahy, J., Field, P., and Furtado, K.: Critical Southern Ocean
976 climate model biases traced to atmospheric model cloud errors, *Nat. Commun.*, 9, 1–17,
977 <https://doi.org/10.1038/s41467-018-05634-2>, 2018.

978 Jacob, D., Petersen, J., Eggert, B., Alias, A., Christensen, O. B., Bouwer, L. M., Braun, A.,
979 Colette, A., Déqué, M., Georgievski, G. and Georgopoulou, E.: EURO-CORDEX: new
980 high-resolution climate change projections for European impact research. *Regional*
981 *Environmental Change*, 14, 563–578, <https://doi.org/10.1007/s10113-013-0499-2>, 2014.

982 Kirtman, B. P., Bitz, C., Bryan, F., Collins, W., Dennis, J., Hearn, N., Kinter, J. L., Loft, R.,
983 Rousset, C., Siqueira, L., and Stan, C.: Impact of ocean model resolution on CCSM climate

984 simulations, *Clim. Dynam.*, 39, 1303–1328, <https://doi.org/10.1007/s00382-012-1500-3>,
985 2012.

986 Kriegler, E., Bauer, N., Popp, A., Humpenöder, F., Leimbach, M., Strefler, J., Baumstark, L.,
987 Bodirsky, B.L., Hilaire, J., Klein, D., and Mouratiadou, I.: Fossil-fueled development
988 (SSP5): An energy and resource intensive scenario for the 21st century. *Global*
989 *Environmental Change*, 42, 297–315, <https://doi.org/10.1016/j.gloenvcha.2016.05.015>,
990 2017.

991 Lee, R.W., Woollings, T. J., Hoskins, B. J., Williams, K. D., O’Reilly, C. H. and Masato, G.:
992 Impact of Gulf Stream SST biases on the global atmospheric circulation. *Climate Dynamics*,
993 51, 3369–3387, <https://doi.org/10.1007/s00382-018-4083-9>, 2018.

994 Lofverstrom, M., Fyke, J. G., Thayer-Calder, K., Muntjewerf, L., Vizcaino, M., Sacks, W. J.,
995 Lipscomb, W. H., Otto-Bliesner, B. L. and Bradley, S. L.: An efficient ice sheet/Earth
996 system model spin-up procedure for CESM2-CISM2: Description, evaluation, and broader
997 applicability. *Journal of Advances in Modeling Earth Systems*, 12(8), e2019MS001984,
998 <https://doi.org/10.1029/2019MS001984>, 2020.

999 Lyu, G., Köhl, A., Matei, I. and Stammer, D.: Adjoint-based climate model tuning:
1000 Application to the planet simulator. *Journal of Advances in Modeling Earth Systems*, 10(1),
1001 207–222, <https://doi.org/10.1002/2017MS001194>, 2018.

1002 Ma, X., Chang, P., Saravanan, R., Montuoro, R., Nakamura, H., Wu, D., Lin, X. and Wu, L.:
1003 Importance of resolving Kuroshio front and eddy influence in simulating the North Pacific
1004 storm track. *Journal of Climate*, 30(5), 1861–1880, [https://doi.org/10.1175/JCLI-D-16-](https://doi.org/10.1175/JCLI-D-16-0154.1)
1005 0154.1, 2017.

1006 Madec, G.: NEMO reference manual, ocean dynamic component: NEMO-OPA, Note du Pôle
1007 modélisation, Inst. Pierre Simon Laplace, France, 2008.

1008 Madec, G. and the NEMO team: NEMO ocean engine version 3.6 stable, Note du Pôle de
1009 modélisation de l’Institut Pierre-Simon Laplace No. 27, ISSN: 1288–1619, 2016.

1010 Manubens-Gil, D., Vegas-Regidor, J., Prodhomme, C., Mula-Valls, O. and Doblas-Reyes, F.
1011 J.: Seamless management of ensemble climate prediction experiments on HPC platforms. In
1012 2016 International Conference on High Performance Computing & Simulation (HPCS),
1013 895–900, 2016, <https://doi.org/10.1109/HPCSim.2016.7568429>, 2016.

1014 Mauritsen, T., Stevens, B., Roeckner, E., Crueger, T., Esch, M., Giorgetta, M., Haak, H.,
1015 Jungclaus, J., Klocke, D., Matei, D. and Mikolajewicz, U.: Tuning the climate of a global
1016 model. *Journal of advances in modeling Earth systems*, 4(3),
1017 <https://doi.org/10.1029/2012MS000154>, 2012.

1018 McDougall, T. J., Barker, P. M., Holmes, R. M., Pawlowicz, R., Griffies, S. M. and Durack,
1019 P. J.: The interpretation of temperature and salinity variables in numerical ocean model
1020 output and the calculation of heat fluxes and heat content. *Geoscientific Model*
1021 *Development*, 14(10), 6445–6466, <https://doi.org/10.5194/gmd-14-6445-2021>, 2021.

1022 McGee, D., Moreno-Chamarro, E., Marshall, J. and Galbraith, E.D.: Western US lake
1023 expansions during Heinrich stadials linked to Pacific Hadley circulation. *Science advances*,
1024 4(11), p.eaav0118, <https://doi.org/10.1126/sciadv.aav0118>, 2018.

1025 Meehl, G.A., Yang, D., Arblaster, J.M., Bates, S.C., Rosenbloom, N., Neale, R., Bacmeister,
1026 J., Lauritzen, P.H., Bryan, F., Small, J. and Truesdale, J.: Effects of model resolution,
1027 physics, and coupling on Southern Hemisphere storm tracks in CESM1. 3. *Geophysical*
1028 *Research Letters*, 46(21), 12408–12416, <https://doi.org/10.1029/2019GL084057>, 2019.

1029 Merlis, T. M. and Khatiwala, S.: Fast dynamical spin-up of ocean general circulation models
1030 using Newton–Krylov methods. *Ocean Modelling*, 21(3-4), 97–105,
1031 <https://doi.org/10.1016/j.ocemod.2007.12.001>, 2008.

1032 Milinski, S., Bader, J., Haak, H., Siongco, A. C., and Jungclaus, J. H.: High atmospheric
1033 horizontal resolution eliminates the wind-driven coastal warm bias in the southeastern
1034 tropical Atlantic: *Geophys. Res. Lett.*, 43, 10455–10462,
1035 <https://doi.org/10.1002/2016GL070530>, 2016.

1036 Monteverde, C., De Sales, F. and Jones, C.: Evaluation of the CMIP6 performance in
1037 simulating precipitation in the Amazon River basin. *Climate*, 10(8), 122,
1038 <https://doi.org/10.3390/cli10080122>, 2022.

1039 Moreno-Chamarro, E.: Data for “The very-high resolution configuration of the EC-Earth
1040 global model for HighResMIP”, Zenodo [data set, last access: 10 July 2024],
1041 <https://doi.org/10.5281/zenodo.12078052>, 2024.

1042 Moreno-Chamarro, E., Caron, L. P., Ortega, P., Tomas, S. L. and Roberts, M. J.: Can we trust
1043 CMIP5/6 future projections of European winter precipitation?: *Environmental Research*
1044 *Letters*, 16(5), 054063, <https://doi.org/10.1088/1748-9326/abf28a>, 2021.

1045 Moreno-Chamarro, E., Caron, L. P., Loosveldt Tomas, S., Vegas-Regidor, J., Gutjahr, O.,
1046 Moine, M. P., Putrasahan, D., Roberts, C. D., Roberts, M. J., Senan, R. and Terray, L.:
1047 Impact of increased resolution on long-standing biases in HighResMIP-PRIMAVERA
1048 climate models: *Geoscientific Model Development*, 15(1), 269–289,
1049 <https://doi.org/10.5194/gmd-15-269-2022>, 2022.

1050 Moreton, S., Ferreira, D., Roberts, M. and Hewitt, H.: Air-Sea Turbulent Heat Flux Feedback
1051 Over Mesoscale Eddies. *Geophysical Research Letters*, 48(20), e2021GL095407,
1052 <https://doi.org/10.1029/2021GL095407>, 2021.

1053 Pawlowicz, R.: Key physical variables in the ocean: temperature, salinity, and density. *Nature*
1054 *Education Knowledge*, 4(4), 13, 2013.

1055 Pershing, A.J., Alexander, M.A., Hernandez, C.M., Kerr, L.A., Le Bris, A., Mills, K.E., Nye,
1056 J.A., Record, N.R., Scannell, H.A., Scott, J.D. and Sherwood, G.D.: Slow adaptation in the
1057 face of rapid warming leads to collapse of the Gulf of Maine cod fishery. *Science*,
1058 350(6262), 809–812, <https://doi.org/10.1126/science.aac9819>, 2015.

1059 PRIMAVERA and the European Commission: Grant Agreement number: 641727 – PRocess-
1060 based climate sIMulation: AdVances in high resolution modelling and European climate
1061 Risk Assessment (PRIMAVERA), Zenodo, <https://doi.org/10.5281/zenodo.3874429>, 2015.

1062 Rai, S., Hecht, M.W., Maltrud, M.E. and Aluie, H.: Scale-dependent Air-Sea Mechanical
1063 Coupling: Resolution Mismatch and Spurious Eddy-Killing,
1064 <https://doi.org/10.22541/essoar.167525271.13326232/v1>, 2023.

1065 Rackow, T., Sein, D. V., Semmler, T., Danilov, S., Koldunov, N. V., Sidorenko, D., Wang,
1066 Q., and Jung, T.: Sensitivity of deep ocean biases to horizontal resolution in prototype
1067 CMIP6 simulations with AWI-CM1.0, *Geosci. Model Dev.*, 12, 2635–2656,
1068 <https://doi.org/10.5194/gmd-12-2635-2019>, 2019.

1069 Rackow, T., Pedruzo-Bagazgoitia, X., Becker, T., Milinski, S., Sandu, I., Aguridan, R.,
1070 Bechtold, P., Beyer, S., Bidlot, J., Boussetta, S., Diamantakis, M., Dueben, P., Dutra, E.,
1071 Forbes, R., Goessling, H. F., Hadade, I., Hegewald, J., Keeley, S., Kluft, L., Koldunov, N.,
1072 Koldunov, A., Kölling, T., Kousal, J., Mogensen, K., Quintino, T., Polichtchouk, I.,
1073 Sármany, D., Sidorenko, D., Streffing, J., Sützl, B., Takasuka, D., Tietsche, S., Valentini,
1074 M., Vannièrè, B., Wedi, N., Zampieri, L., and Ziemer, F.: Multi-year simulations at

1075 kilometre scale with the Integrated Forecasting System coupled to FESOM2.5/NEMOv3.4,
1076 EGUsphere [preprint], <https://doi.org/10.5194/egusphere-2024-913>, 2024.

1077 Renault, L., Lemarié, F. and Arsouze, T.: On the implementation and consequences of the
1078 oceanic currents feedback in ocean–atmosphere coupled models. *Ocean Modelling*, 141,
1079 101423, <https://doi.org/10.1016/j.ocemod.2019.101423>, 2019.

1080 Renault, L., Marchesiello, P., & Contreras, M.: Coaction of top and bottom drags in Gulf
1081 Stream dynamics. *Journal of Geophysical Research: Oceans*, 128, e2022JC018939.
1082 <https://doi.org/10.1029/2022JC018939>, 2023.

1083 Richter, I.: Climate model biases in the eastern tropical oceans: Causes, impacts and ways
1084 forward, *Wires Clim. Change*, 6, 345–358, <https://doi.org/10.1002/wcc.338>, 2015.

1085 Roberts, C. D., Senan, R., Molteni, F., Boussetta, S., Mayer, M., and Keeley, S. P. E.: Climate
1086 model configurations of the ECMWF Integrated Forecasting System (ECMWF-IFS cycle
1087 43r1) for HighResMIP, *Geosci. Model Dev.*, 11, 3681–3712, [https://doi.org/10.5194/gmd-](https://doi.org/10.5194/gmd-11-3681-2018)
1088 [11-3681-2018](https://doi.org/10.5194/gmd-11-3681-2018), 2018.

1089 Roberts, M. J., Baker, A., Blockley, E. W., Calvert, D., Coward, A., Hewitt, H. T., Jackson, L.
1090 C., Kuhlbrodt, T., Mathiot, P., Roberts, C. D. and Schiemann, R.: Description of the
1091 resolution hierarchy of the global coupled HadGEM3-GC3. 1 model as used in CMIP6
1092 HighResMIP experiments. *Geoscientific Model Development*, 12(12), 4999–5028,
1093 <https://doi.org/10.5194/gmd-12-4999-2019>, 2019.

1094 Roberts, M. J., Camp, J., Seddon, J., Vidale, P. L., Hodges, K., Vanniere, B., Mecking, J.,
1095 Haarsma, R., Bellucci, A., Scoccimarro, E., and Caron, L. P.: Impact of model resolution on
1096 tropical cyclone simulation using the HighResMIP–PRIMAVERA multimodel ensemble, *J.*
1097 *Climate*, 33, 2557–2583, <https://doi.org/10.1175/JCLI-D-19-0639.1>, 2020a.

1098 Roberts, M. J., Jackson, L. C., Roberts, C. D., Meccia, V., Docquier, D., Koenigk, T., Ortega,
1099 P., Moreno-Chamarro, E., Bellucci, A., Coward, A., and Drijfhout, S.: Sensitivity of the
1100 Atlantic meridional overturning circulation to model resolution in CMIP6 HighResMIP
1101 simulations and implications for future changes, *J. Adv. Model. Earth Sy.*, 12,
1102 e2019MS002014, <https://doi.org/10.1029/2019MS002014>, 2020b.

1103 Roberts, M. J., Vidale, P. L., Senior, C., Hewitt, H. T., Bates, C., Berthou, S., Chang, P.,
1104 Christensen, H. M., Danilov, S., Demory, M. E., and Griffies, S. M.: The benefits of global
1105 high resolution for climate simulation: process understanding and the enabling of

1106 stakeholder decisions at the regional scale, *B. Am. Meteorol. Soc.*, 99, 2341–2359,
1107 <https://doi.org/10.1175/BAMS-D-15-00320.1>, 2018.

1108 Saba, V.S., Griffies, S.M., Anderson, W.G., Winton, M., Alexander, M.A., Delworth, T.L.,
1109 Hare, J.A., Harrison, M.J., Rosati, A., Vecchi, G.A. and Zhang, R.: Enhanced warming of
1110 the Northwest Atlantic Ocean under climate change. *Journal of Geophysical Research:*
1111 *Oceans*, 121(1), 118–132, <https://doi.org/10.1002/2015JC011346>, 2016.

1112 Sarmany, D., Valentini, M., Maciel, P., Geier, P., Smart, S., Aguridan, R., Hawkes, J. and
1113 Quintino, T.: MultiIO: A Framework for Message-Driven Data Routing For Weather and
1114 Climate Simulations. *Proceedings of the Platform for Advanced Scientific Computing*
1115 *Conference*, 1–12, <https://doi.org/10.1145/3659914.365993>, 2024.

1116 Segura, H., Hohenegger, C., Wengel, C. and Stevens, B.: Learning by doing: Seasonal and
1117 diurnal features of tropical precipitation in a global-coupled storm-resolving model.
1118 *Geophysical Research Letters*, 49(24), p.e2022GL101796,
1119 <https://doi.org/10.1029/2022GL101796>, 2022.

1120 Sein, D. V., Koldunov, N. V., Danilov, S., Wang, Q., Sidorenko, D., Fast, I., Rackow, T.,
1121 Cabos, W. and Jung, T.: Ocean modeling on a mesh with resolution following the local
1122 Rossby radius. *Journal of Advances in Modeling Earth Systems*, 9(7), 2601–2614,
1123 <https://doi.org/10.1002/2017MS001099>, 2017.

1124 Semmler, T., Danilov, S., Gierz, P., Goessling, H. F., Hegewald, J., Hinrichs, C., Koldunov,
1125 N., Khosravi, N., Mu, L., Rackow, T. and Sein, D. V.: Simulations for CMIP6 with the AWI
1126 climate model AWI-CM-1-1. *Journal of Advances in Modeling Earth Systems*, 12(9),
1127 <https://doi.org/10.1029/2019MS002009>, 2020.

1128 Small, R.J., Bacmeister, J., Bailey, D., Baker, A., Bishop, S., Bryan, F., Caron, J., Dennis, J.,
1129 Gent, P., Hsu, H.M. and Jochum, M.: A new synoptic scale resolving global climate
1130 simulation using the Community Earth System Model. *Journal of Advances in Modeling*
1131 *Earth Systems*, 6(4), 1065–1094, <https://doi.org/10.1002/2014MS000363>, 2014.

1132 Small, R. J., Bryan, F. O., Bishop, S. P., and Tomas, R. A.: Air–sea turbulent heat fluxes in
1133 climate models and observational analyses: What drives their variability?. *Journal of*
1134 *Climate*, 32(8), 2397–2421, <https://doi.org/10.1175/JCLI-D-18-0576.1>, 2019.

1135 Soufflet, Y., Marchesiello, P., Lemarié, F., Jouanno, J., Capet, X., Debreu, L., and Benshila,
1136 R.: On effective resolution in ocean models. *Ocean Modelling*, 98, 36–50,
1137 <https://doi.org/10.1016/j.ocemod.2015.12.004>, 2016.

1138 Stengel, M., Stapelberg, S., Sus, O., Finkensieper, S., Würzler, B., Philipp, D., Hollmann, R.,
1139 Poulsen, C., Christensen, M., and McGarragh, G.: Cloud_cci Advanced Very High
1140 Resolution Radiometer post meridiem (AVHRR-PM) dataset version 3: 35 year climatology
1141 of global cloud and radiation properties, *Earth Syst. Sci. Data*, 12, 41–60,
1142 <https://doi.org/10.5194/essd-12-41-2020>, 2020 (data available at:
1143 <https://climate.esa.int/en/projects/cloud/data/>, last access: 10 March 2021).

1144 Sun, X. and Wu, R.: Spatial scale dependence of the relationship between turbulent surface
1145 heat flux and SST. *Climate Dynamics*, 58(3), 1127–1145, [https://doi.org/10.1007/s00382-](https://doi.org/10.1007/s00382-021-05957-9)
1146 [021-05957-9](https://doi.org/10.1007/s00382-021-05957-9), 2022.

1147 Tian, B. and Dong, X.: The double-ITCZ bias in CMIP3, CMIP5, and CMIP6 models based
1148 on annual mean precipitation, *Geophys. Res. Lett.*, 47, e2020GL087232,
1149 <https://doi.org/10.1029/2020GL087232>, 2020.

1150 Tintó, O., Acosta, M., Castrillo, M., Cortés, A., Sanchez, A., Serradell, K., and Doblas-Reyes,
1151 F. J.: Optimizing domain decomposition in an ocean model: the case of NEMO, *Procedia*
1152 *Comput. Sci.*, 108, 776–785, 2017.

1153 Tintó, O., M. C. Acosta, A. M. Moore, M. Castrillo, K. Serradell, A. Cortés and F. J. Doblas-
1154 Reyes: How to use mixed precision in ocean models: exploring a potential reduction of
1155 numerical precision in NEMO 4.0 and ROMS 3.6. *Geoscientific Model Development*, 12,
1156 3135-3148, <https://doi.org/10.5194/gmd-12-3135-2019>, 2019a.

1157 Tintó, O., M. Castrillo, M. C. Acosta, O. Mula-Valls, A. Sanchez Lorente, K. Serradell, A.
1158 Cortés and F. J. Doblas-Reyes: Finding, analysing and solving MPI communication
1159 bottlenecks in Earth System models. *Journal of Computational Sciences*, 36, 100864,
1160 <https://doi.org/10.1016/j.jocs.2018.04.015>, 2019b.

1161 Todd, R. E. and Ren, A. S.: Warming and lateral shift of the Gulf Stream from in situ
1162 observations since 2001. *Nature Climate Change*, 13(12), 1348–1352,
1163 <https://doi.org/10.1038/s41558-023-01835-w>, 2023.

1164 Tomita, H., Hihara, T., Kako, S.I., Kubota, M. and Kutsuwada, K.: An introduction to J-
1165 OFURO3, a third-generation Japanese ocean flux data set using remote-sensing

1166 observations. *Journal of Oceanography*, 75(2), 171–194, <https://doi.org/10.1007/s10872->
1167 018-0493-x, 2019 (data available at: <https://www.j-ofuro.com/en/dataset/>, last access: 14
1168 March 2024).

1169 Tsartsali, E. E., Haarsma, R. J., Athanasiadis, P. J., Bellucci, A., de Vries, H., Drijfhout, S., de
1170 Vries, I. E., Putrahasan, D., Roberts, M. J., Sanchez–Gomez, E. and Roberts, C. D.: Impact
1171 of resolution on the atmosphere–ocean coupling along the Gulf Stream in global high
1172 resolution models. *Climate Dynamics*, 58(11–12), 3317–3333,
1173 <https://doi.org/10.1007/s00382-021-06098-9>, 2022.

1174 Valcke, S. and Morel, T.: OASIS and PALM, the CERFACS couplers, Tech. rep., CERFACS,
1175 2006.

1176 Váňa, F., Düben, P., Lang, S., Palmer, T., Leutbecher, M., Salmond, D. and Carver, G.: Single
1177 precision in weather forecasting models: An evaluation with the IFS. *Monthly Weather*
1178 *Review*, 145(2), 495–502, <https://doi.org/10.1175/MWR-D-16-0228.1>, 2017.

1179 Vancoppenolle, M., Bouillon, S., Fichefet, T., Goosse, H., Lecomte, O., Morales Maqueda,
1180 M. A., and Madec, G.: The Louvain-la-Neuve sea ice model, Notes du pole de modélisation,
1181 Institut Pierre-Simon Laplace (IPSL), Paris, France, No. 31, 2012.

1182 Varma, V., Morgenstern, O., Field, P., Furtado, K., Williams, J., and Hyder, P.: Improving the
1183 Southern Ocean cloud albedo biases in a general circulation model, *Atmos. Chem. Phys.*,
1184 20, 7741–7751, <https://doi.org/10.5194/acp-20-7741-2020>, 2020.

1185 Vidale, P. L., Hodges, K., Vannièrè, B., Davini, P., Roberts, M. J., Strommen, K.,
1186 Weisheimer, A., Plesca, E., and Corti, S.: Impact of stochastic physics and model resolution
1187 on the simulation of Tropical Cyclones in climate GCMs, *J. Climate*, 34, 4315–4341,
1188 <https://doi.org/10.1175/JCLI-D-20-0507.1>, 2021.

1189 Wan, H., Rasch, P. J., Zhang, K., Qian, Y., Yan, H. and Zhao, C.: Short ensembles: An
1190 efficient method for discerning climate-relevant sensitivities in atmospheric general
1191 circulation models. *Geoscientific Model Development*, 7(5), 1961–1977,
1192 <https://doi.org/10.5194/gmd-7-1961-2014>, 2014.

1193 Wengel, C., Lee, S. S., Stuecker, M. F., Timmermann, A., Chu, J. E., and Schloesser, F.:
1194 Future high-resolution El Niño/Southern Oscillation dynamics, *Nat. Clim. Change*, 1–8,
1195 <https://doi.org/10.1038/s41558-021-01132-4>, 2021.

1196 Williamson, D., Goldstein, M., Allison, L., Blaker, A., Challenor, P., Jackson, L. and
1197 Yamazaki, K.: History matching for exploring and reducing climate model parameter space
1198 using observations and a large perturbed physics ensemble. *Climate Dynamics*, 41, 1703–
1199 1729, <https://doi.org/10.1007/s00382-013-1896-4>, 2013.

1200 Woollings, T., Hoskins, B., Blackburn, M., Hassell, D. and Hodges, K.: Storm track
1201 sensitivity to sea surface temperature resolution in a regional atmosphere model. *Climate*
1202 *Dynamics*, 35, 341–353, <https://doi.org/10.1007/s00382-009-0554-3>, 2010.

1203 Xepes-Arbós, X., G. van den Oord, M. C. Acosta and G. D. Carver: Evaluation and
1204 optimisation of the I/O scalability for the next generation of Earth system models: IFS
1205 CY43R3 and XIOS 2.0 integration as a case study. *Geoscientific Model Development*, 15,
1206 379–394, <https://doi.org/10.5194/gmd-15-379-2022>, 2022.

1207 Zhang, J. and Rothrock, D. A.: Modeling global sea ice with a thickness and enthalpy
1208 distribution model in generalized curvilinear coordinates, *Mon. Weather Rev.*, 131, 845–
1209 861, [https://doi.org/10.1175/1520-0493\(2003\)131<0845:Mgsiwa>2.0.Co;2](https://doi.org/10.1175/1520-0493(2003)131<0845:Mgsiwa>2.0.Co;2), 2003 (data
1210 available at: https://psc.apl.washington.edu/zhang/Global_seaice/model.html, last access: 6
1211 March 2019).

1212 Zhang, W., Villarini, G., Scoccimarro, E., Roberts, M., Vidale, P. L., Vanniere, B., Caron, L.
1213 P., Putrasahan, D., Roberts, C., Senan, R., and Moine, M. P.: Tropical cyclone precipitation
1214 in the HighResMIP atmosphere-only experiments of the PRIMAVERA Project, *Clim.*
1215 *Dynam.*, 57, 253–273, <https://doi.org/10.1007/s00382-021-05707-x>, 2021.